

AD-A130 956

RADIATION PATTERNS OF AN ANTENNA MOUNTED ON THE OFF-MID 1/1  
SECTION OF AN ELLIPSOID(U) OHIO STATE UNIV COLUMBUS

UNCLASSIFIED

ELECTROSCIENCE LAB J G KIM ET AL. JUN 83 ESL-714215-3  
N00019-81-C-0424

F/G 20/14

NL

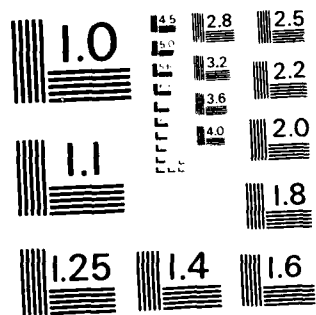
END

DATE

FILMED

BY JHS

DTIC



MICROCOPY RESOLUTION TEST CHART  
NATIONAL BUREAU OF STANDARDS-1963-A

OSU

The Ohio State University

RADIATION PATTERNS OF AN ANTENNA MOUNTED ON THE  
OFF-MID SECTION OF AN ELLIPSOID

Jeung G. Kim  
Walter D. Burnside

The Ohio State University

**ElectroScience Laboratory**

Department of Electrical Engineering  
Columbus, Ohio 43212

Quarterly Report 714215-3  
Contract No. N00019-81-C-0424  
June 1983

DTIC  
ELECTE  
JUL 29 1983  
S B

APPROVED FOR PUBLIC RELEASE:  
DISTRIBUTION UNLIMITED

Department of the Navy  
Naval Air Systems Command  
Washington, D.C. 20361

83 07 29 010

AD A130956

DTIC FILE COPY

## NOTICES

When Government drawings, specifications, or other data are used for any purpose other than in connection with a definitely related Government procurement operation, the United States Government thereby incurs no responsibility nor any obligation whatsoever, and the fact that the Government may have formulated, furnished, or in any way supplied the said drawings, specifications, or other data, is not to be regarded by implication or otherwise as in any manner licensing the holder or any other person or corporation, or conveying any rights or permission to manufacture, use, or sell any patented invention that may in any way be related thereto.

REPORT DOCUMENTATION PAGE		1. REPORT NO. <i>AD A130 956</i>	2.	3. Recipient's Accession No.
4. Title and Subtitle RADIATION PATTERNS OF AN ANTENNA MOUNTED ON THE OFF-MID SECTION OF AN ELLIPSOID		5. Report Date June 1983		6.
7. Author(s) Jeung G. Kim and Walter D. Burnside		8. Performing Organization Report No. ESL 714215-3		9.
9. Performing Organization Name and Address The Ohio State University ElectroScience Laboratory Department of Electrical Engineering Columbus, Ohio 43212		10. Project/Task/Work Unit No.		11. Contract(C) or Grant(G) No. (C) (G) N00019-81-C-0424
12. Sponsoring Organization Name and Address Department of the Navy Naval Air Systems Command Washington, D.C. 20361		13. Type of Report & Period Covered Quarterly Report		14.
15. Supplementary Notes <i>(This is a preliminary report)</i>				
16. Abstract (Limit 200 words) An efficient numerical solution for the high frequency radiation patterns of an Antenna mounted on the Off-Mid Section ( $\theta_s \neq 90^\circ$ ) of an Ellipsoid is studied in this report. The Uniform Geometrical Theory of Diffraction (UTD) [1] is the basic approach applied here and the elliptic cone perturbation method [2,3] is used to simulate geodesic paths on the ellipsoid surface. The radiation patterns obtained using this technique are compared to those for prolate spheroid-mounted antennas, which have shown good agreement with measured data. Exact agreement between both results for typical spheroid geometries confirms that radiation patterns for ellipsoid mounted antennas can be solved efficiently by this numerical technique.				
17. Document Analysis a. Descriptors				
b. Identifiers/Open-Ended Terms				
c. COSATI Field/Group				
18. Availability Statement APPROVED FOR PUBLIC RELEASE DISTRIBUTION UNLIMITED		19. Security Class (This Report) Unclassified		21. No. of Pages 62
		20. Security Class (This Page) Unclassified		22. Price

(See ANSI-Z39.18)

See Instructions on Reverse

 OPTIONAL FORM 272 (4-77)  
 (Formerly NTIS-35)  
 Department of Commerce

# TABLE OF CONTENTS

	Page
LIST OF FIGURES	iii
I. INTRODUCTION	1
II. NUMERICAL TECHNIQUE	1
A. INTRODUCTION	1
B. NUMERICAL APPROACH FOR PATTERN CALCULATION	2
III. RESULTS	18
IV. CONCLUSIONS	21
REFERENCES	62



✓	
Dist	A

# LIST OF FIGURES

Figure		Page
1.	Geodesic path from the source on an ellipsoid.	3
2.	Geodesic path on a developed elliptic cone.	7
3.	Illustration of the diffraction point finding for a given receiver location.	15
4.	Illustration of the divergence factor ( $\sqrt{d\psi_0/d\psi}$ ) terms.	17
5.	Definition of pattern axis.	19
6.	Various source locations tested.	20
7.	Comparison of radiation patterns for $R_t = 15\lambda$ for a short monopole mounted at $\phi_s = 0^\circ$ , $\theta_s = 60^\circ$ on a $2\lambda \times 10\lambda$ spheriod.	23
8.	Comparison of radiation patterns for a short monopole mounted at $\phi_s = 0^\circ$ , $\theta_s = 30^\circ$ on a $2\lambda \times 10\lambda$ spheriod.	25
9.	Comparison of radiation patterns for a short monopole mounted at $\phi_s = 30^\circ$ , $\theta_s = 60^\circ$ on a $2\lambda \times 10\lambda$ spheriod.	27
10.	Comparison of radiation patterns for a short monopole mounted at $\phi_s = 30^\circ$ , $\theta_s = 30^\circ$ on a $2\lambda \times 10\lambda$ spheriod.	29
11.	Comparison of radiation patterns for a short monopole mounted at $\phi_s = 30^\circ$ , $\theta_s = 120^\circ$ on a $2\lambda \times 10\lambda$ spheriod.	31
12.	Comparison of radiation patterns for an axial slot mounted at $\phi_s = 0^\circ$ , $\theta_s = 60^\circ$ on a $2\lambda \times 10\lambda$ spheriod.	33

Figure		Page
13.	Comparison of radiation patterns for an axial slot mounted at $\phi_S = 0^\circ$ , $\theta_S = 30^\circ$ on a $2\lambda \times 10\lambda$ spheroid.	35
14.	Comparison of radiation patterns for an axial slot mounted at $\phi_S = 30^\circ$ , $\theta_S = 60^\circ$ on a $2\lambda \times 10\lambda$ spheroid.	37
15.	Comparison of radiation patterns for an axial slot mounted at $\phi_S = 30^\circ$ , $\theta_S = 30^\circ$ on a $2\lambda \times 10\lambda$ spheroid.	39
16.	Comparison of radiation patterns for a circumferential slot mounted at $\phi_S = 0^\circ$ , $\theta_S = 60^\circ$ on a $2\lambda \times 10\lambda$ spheroid.	41
17.	Comparison of radiation patterns for a circumferential slot mounted at $\phi_S = 0^\circ$ , $\theta_S = 30^\circ$ on a $2\lambda \times 10\lambda$ spheroid.	43
18.	Comparison of radiation patterns for a circumferential slot mounted at $\phi_S = 30^\circ$ , $\theta_S = 60^\circ$ on a $2\lambda \times 10\lambda$ spheroid.	45
19.	Comparison of radiation patterns for a circumferential slot mounted at $\phi_S = 30^\circ$ , $\theta_S = 30^\circ$ on a $2\lambda \times 10\lambda$ spheroid.	47
20.	Radiation patterns for $R_t = 15\lambda$ for a short monopole mounted at $\phi_S = 0^\circ$ , $\theta_S = 60^\circ$ on a $2\lambda \times 4\lambda \times 10\lambda$ ellipsoid.	49
21.	Radiation patterns for a short monopole mounted at $\phi_S = 0^\circ$ , $\theta_S = 30^\circ$ on a $2\lambda \times 4\lambda \times 10\lambda$ ellipsoid.	50
22.	Radiation patterns for a short monopole mounted at $\phi_S = 30^\circ$ , $\theta_S = 60^\circ$ on a $2\lambda \times 4\lambda \times 10\lambda$ ellipsoid.	51
23.	Radiation patterns for a short monopole mounted at $\phi_S = 30^\circ$ , $\theta_S = 30^\circ$ on a $2\lambda \times 4\lambda \times 10\lambda$ ellipsoid.	52
24.	Radiation patterns for an axial slot mounted at $\phi_S = 0^\circ$ , $\theta_S = 60^\circ$ on a $2\lambda \times 4\lambda \times 10\lambda$ ellipsoid.	53



Figure		Page
25.	Radiation patterns for an axial slot mounted at $\phi_s = 0^\circ$ , $\theta_s = 30^\circ$ on a $2\lambda \times 4\lambda \times 10\lambda$ ellipsoid.	54
26.	Radiation patterns for an axial slot mounted at $\phi_s = 30^\circ$ , $\theta_s = 60^\circ$ on a $2\lambda \times 4\lambda \times 10\lambda$ ellipsoid.	55
27.	Radiation patterns for an axial slot mounted at $\phi_s = 30^\circ$ , $\theta_s = 30^\circ$ on a $2\lambda \times 4\lambda \times 10\lambda$ ellipsoid.	56
28.	Radiation patterns for a circumferential slot mounted at $\phi_s = 0^\circ$ , $\theta_s = 60^\circ$ on a $2\lambda \times 4\lambda \times 10\lambda$ ellipsoid.	57
29.	Radiation patterns for a circumferential slot mounted at $\phi_s = 0^\circ$ , $\theta_s = 30^\circ$ on a $2\lambda \times 4\lambda \times 10\lambda$ ellipsoid.	58
30.	Radiation patterns for a circumferential slot mounted at $\phi_s = 30^\circ$ , $\theta_s = 60^\circ$ on a $2\lambda \times 4\lambda \times 10\lambda$ ellipsoid.	59
31.	Radiation patterns for a circumferential slot mounted at $\phi_s = 30^\circ$ , $\theta_s = 30^\circ$ on a $2\lambda \times 4\lambda \times 10\lambda$ ellipsoid.	60
32.	Cone boundary used to define terms to be included in the shadow region.	61

## I. INTRODUCTION

In applying the Uniform Geometrical Theory of Diffraction (UTD) to antenna radiation problem involving curved surfaces, a major task is to determine the final diffraction point and the geodesic path on the curved surface. For the antennas mounted on the fuselage of an aircraft, the fuselage can be modeled as an ellipsoid in the UTD analysis. Geodesic paths on an ellipsoid have been studied in detail in References [2,3] using an elliptic cone perturbation method which is very efficient.

Using this perturbation method and another numerical technique, which will be given in this report, the radiation patterns for ellipsoid mounted antennas is efficiently obtained. The theoretical UTD concept to calculate actual radiation fields is given in References [1,2].

## II. NUMERICAL TECHNIQUE

### A. INTRODUCTION

The ellipsoid simulated by a perturbed elliptic cone model is examined here. Since the elliptic cone is a developable surface, geodesics can be easily obtained [2,3]. Given a radiation direction  $(\theta_t, \phi_t)$ , one can find the final diffraction point  $(\theta_q, \phi_q)$  by following the geodesic path, step by step, until the geodesic tangent coincides

with the radiation direction  $(\theta_t, \phi_t)$ . This is a rather tedious and time consuming process if applied for each new radiation direction.

Considering a new radiation direction, which does not deviate greatly from the previous direction, one should be able to develop a solution which uses the properties of the surface and the previous geodesic path to find the new diffraction point. Such an approach is attempted here to make this solution as efficient as possible.

Since the field decays exponentially along the ray path on the surface, it is assumed that only one or possibly two dominant rays exist in the problems treated. One is referred to References [2,3] for more details on this topic.

#### B. NUMERICAL APPROACH FOR PATTERN CALCULATION

Assuming the diffraction point is located at  $Q (a \cos v_e \cos v_r, b \cos v_e \sin v_r, c \sin v_e)$  and the field point at  $P (R_t \sin \theta_t \cos \phi_t, R_t \sin \theta_t \sin \phi_t, R_t \cos \theta_t)$ , then at the diffraction point  $Q$  the radiation direction  $(\theta_t, \phi_t)$  should coincide with the geodesic tangent  $\hat{t}$  as shown in Figure 1. Thus,

$$\begin{aligned}\hat{t} &= \hat{x} t_x + \hat{y} t_y + \hat{z} t_z \\ &= \hat{t}_1 \cos \beta + \hat{t}_e \sin \beta,\end{aligned}$$

where

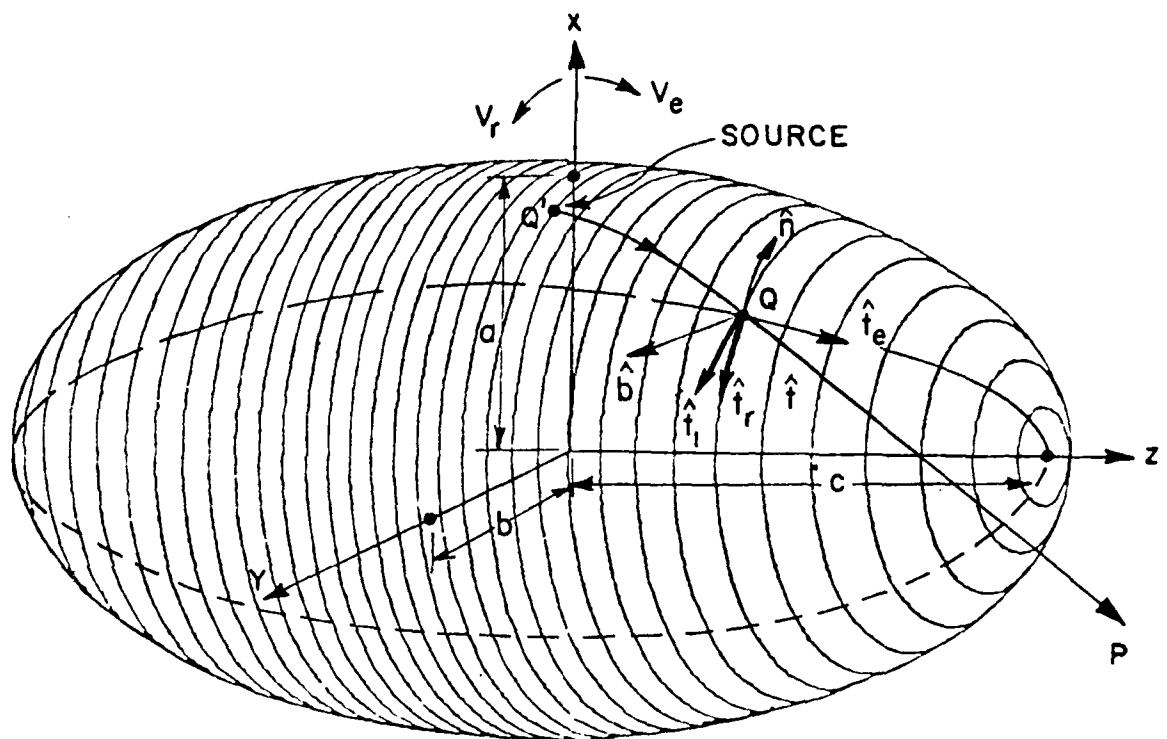


Figure 1. Geodesic path from the source on an ellipsoid.

$$t_x = \frac{\sin \theta_t \cos \phi_t - \frac{a}{R_t} \cos v_e \cos v_r}{D}$$

$$t_y = \frac{\sin \theta_t \sin \phi_t - \frac{b}{R_t} \cos v_e \cos v_r}{D}$$

and

$$t_z = \frac{\cos \theta_t - \frac{c}{R_t} \sin v_e}{D}.$$

Note that

$$\begin{aligned} D^2 &= \left( \sin \theta_t \cos \phi_t - \frac{a}{R_t} \cos v_e \cos v_r \right)^2 + \left( \sin \theta_t \sin \phi_t - \frac{b}{R_t} \cos v_e \sin v_r \right)^2 + \left( \cos \theta_t - \frac{c}{R_t} \sin v_e \right)^2 \\ &= 1 - 2 \left[ \sin \theta_t \cos v_e \left( \frac{a}{R_t} \cos \phi_t \cos v_r + \frac{b}{R_t} \sin \phi_t \sin v_r \right) + \frac{c}{R_t} \cos \theta_t \sin v_e \right] + \left[ \cos^2 v_e \left( \frac{a^2}{R_t^2} \cos^2 v_r + \frac{b^2}{R_t^2} \sin^2 v_r \right) + \frac{c^2}{R_t^2} \sin^2 v_e \right] \end{aligned}$$

, and

$$\begin{aligned} \hat{t}_1 &= \hat{t}_e \times \hat{n} \\ &= \frac{-\hat{x} \sin v_r (b^2 \sin^2 v_e + c^2 \cos^2 v_e) + \hat{y} b \cos v_r (a^2 \sin^2 v_e + c^2 \cos^2 v_e)}{[a^2 b^2 \sin^2 v_e + c^2 \cos^2 v_e (a^2 \sin^2 v_r + b^2 \cos^2 v_r)]^{1/2}} - - \\ &- - - \frac{+\hat{z} c (b^2 - a^2) \sin v_r \cos v_r \sin v_e \cos v_e}{[c^2 \cos^2 v_e + \sin^2 v_e (a^2 \cos^2 v_r + b^2 \sin^2 v_r)]^{1/2}} \end{aligned}$$

where

$$\hat{t}_e = \frac{\frac{\partial R}{\partial v_e}}{\left| \frac{\partial R}{\partial v_e} \right|} = \frac{-\hat{x}a \sin v_e \cos v_r - \hat{y}b \sin v_e \sin v_r + \hat{z}c \cos v_e}{[a^2 \sin^2 v_e \cos^2 v_r + b^2 \sin^2 v_e \sin^2 v_r + c^2 \cos^2 v_e]^{1/2}}$$

$$\hat{t}_r = \frac{\frac{\partial R}{\partial v_r}}{\left| \frac{\partial R}{\partial v_r} \right|} = \frac{-\hat{x}a \cos v_e \sin v_r + \hat{y}b \cos v_e \cos v_r}{[a^2 \cos^2 v_e \sin^2 v_r + b^2 \cos^2 v_e \cos^2 v_r]^{1/2}}$$

and

$$\begin{aligned} n &= \frac{\hat{t}_r \times \hat{t}_e}{|\hat{t}_r \times \hat{t}_e|} \\ &= \frac{\hat{x}bc \cos v_e \cos v_r + \hat{y}ac \cos v_e \sin v_r + \hat{z}ab \sin v_e}{[a^2 b^2 \sin^2 v_e + c^2 \cos^2 v_e (a^2 \sin^2 v_r + b^2 \cos^2 v_r)]^{1/2}} \end{aligned}$$

Equating the x-, y-, and z- components, respectively, one obtains

$$\begin{aligned} t_x &= \frac{-a \sin v_r \cos \beta (b^2 \sin^2 v_e + c^2 \cos^2 v_e)}{[a^2 b^2 \sin^2 v_e + c^2 \cos^2 v_e (a^2 \sin^2 v_r + b^2 \cos^2 v_r)]^{1/2}} \cdot [c^2 \cos^2 v_e + \sin^2 v_e (a^2 \cos^2 v_r + b^2 \sin^2 v_r)]^{1/2} \\ &\quad - \frac{a \sin v_e \cos v_r \sin \beta}{[c^2 \cos^2 v_e + \sin^2 v_e (a^2 \cos^2 v_r + b^2 \sin^2 v_r)]^{1/2}} \\ &= \frac{\sin^2 \theta_t \cos \phi_t - \frac{a}{R_t} \cos v_e \cos v_r}{n} \end{aligned} \quad (1)$$

$$\begin{aligned}
t_y &= \frac{b \cos v_r \cos \beta (a^2 \sin^2 v_e + c^2 \cos v_e)}{[a^2 b^2 \sin^2 v_e + c^2 \cos^2 v_e (a^2 \sin^2 v_r + b^2 \cos^2 v_r)]^{1/2}} \cdot \\
&\quad \cdot [c^2 \cos^2 v_e + \sin^2 v_e (a^2 \cos^2 v_r + b^2 \sin^2 v_r)]^{1/2} \\
&\quad - \frac{b \sin v_e \sin v_r \sin \beta}{[c^2 \cos^2 v_e + \sin^2 v_e (a^2 \cos^2 v_r + b^2 \sin^2 v_r)]^{1/2}} \\
&= \frac{\sin^2 \theta_t \sin \theta_t - \frac{b}{R_t} \cos v_e \sin v_r}{0} \quad (2)
\end{aligned}$$

$$\begin{aligned}
t_z &= \frac{c(b^2 - a^2) \sin v_r \cos v_r \sin v_e \cos v_e \cos \beta}{[a^2 b^2 \sin^2 v_e + c^2 \cos^2 v_e (a^2 \sin^2 v_r + b^2 \cos^2 v_r)]^{1/2}} \cdot \\
&\quad \cdot [c^2 \cos^2 v_e + \sin^2 v_e (a^2 \cos^2 v_r + b^2 \sin^2 v_r)]^{1/2} \\
&\quad + \frac{c \cos v_e \sin \beta}{[c^2 \cos^2 v_e + \sin^2 v_e (a^2 \cos^2 v_r + b^2 \sin^2 v_r)]^{1/2}} \\
&= \frac{\cos^2 \theta_t - \frac{c}{R_t} \sin v_e}{0} \quad (3)
\end{aligned}$$

When the source is located at the off-mid section ( $z \neq 0$  in Figure 1), the ellipsoid is modeled by a perturbed elliptic cone. The associated unfolded surface is shown in Figure 2(b). If  $\gamma$  and  $\beta$  denote the angle between  $\hat{t}$  and  $\hat{t}_1$  at  $Q'$  and  $Q$ , respectively, it is seen that  $\beta = \gamma - \alpha$ . With some manipulation, one can show that the perturbed geodesic path can be expressed as follows:





$$r_e \cos (\gamma - \alpha) = r_s \cos \gamma \quad (4)$$

where

$$\alpha(V_r) = \int_{V_{rS}}^{V_r} \frac{[a_s^2 h_s^2 + Z_s^2 \cot^4 V_{eS} (a_s^2 \sin^2 V_r' + b_s^2 \cos^2 V_r')]^{1/2}}{a_s^2 \cos^2 V_r' + b_s^2 \sin^2 V_r' + Z_s^2 \cot^4 V_{eS}} dV_r' ,$$

$$a_s = a \cos V_{eS} , \quad b_s = b \cos V_{eS} , \quad Z_s = c \sin V_{eS} ,$$

$$r_s = (a_s^2 \cos^2 V_{rS} + b_s^2 \sin^2 V_{rS} + Z_s^2 \cot^4 V_{eS})^{1/2} ,$$

$$r_e = (a_s^2 \cos^2 V_r + b_s^2 \sin^2 V_r + Z_s^2 \cot^4 V_{eS})^{1/2} - S_e ,$$

and

$$S_e = \int_{V_{eS}}^{V_e} [c^2 \cos^2 V_e' + (a^2 \cos^2 V_r + b^2 \sin^2 V_r) \sin^2 V_e']^{1/2} dV_e' .$$

Now,  $[t_x (-b \sin V_r) + t_y a \cos V_r]$  yields

$$\begin{aligned} & \frac{ab \cos(\gamma - \alpha) [c^2 \cos^2 V_e + \sin^2 V_e (a^2 \cos^2 V_r + b^2 \sin^2 V_r)]^{1/2}}{[a^2 h^2 \sin^2 V_e + c^2 \cos^2 V_e (a^2 \sin^2 V_r + b^2 \cos^2 V_r)]^{1/2}} \\ &= \frac{\sin \theta_t (a \cos V_r \sin \phi_t - b \sin V_r \cos \phi_t)}{D} . \end{aligned} \quad (5)$$

Next,  $\{[t_x b \cos V_r + t_y a \sin V_r] c \cos V_e + t_z a b \sin V_e\}$  yields

$$\frac{a \sin V_e \cos \theta_t + c \sin \theta_t \cos V_e (a \sin \phi_t \sin V_r + b \cos \phi_t \cos V_r)}{D}$$

$$- \frac{abc}{DR_t} = 0 \quad . \quad (6)$$

Three functions can, then, be constructed as follows from Equations (4)-(6):

$$F(V_e, V_r, \gamma) = r_e \cos(\gamma - \alpha) - r_s \cos \gamma = 0 \quad . \quad (7)$$

$$\begin{aligned} G(R_t, \theta_t, \phi_t, V_e, V_r, \gamma) \\ &= D a b \cos(\gamma - \alpha) [c^2 \cos^2 V_e + \sin^2 V_e (a^2 \cos^2 V_r + b^2 \sin^2 V_r)]^{1/2} \\ &- \sin \theta_t (a \sin \phi_t \cos V_r - b \cos \phi_t \sin V_r) \cdot \\ &\cdot [a^2 b^2 \sin^2 V_e + c^2 \cos^2 V_e (a^2 \sin^2 V_r + b^2 \cos^2 V_r)]^{1/2} \\ &= 0 \quad . \quad (8) \end{aligned}$$

Further, one finds that

$$\begin{aligned} H(R_t, \theta_t, \phi_t, V_e, V_r) \\ &= a \sin V_e \cos \theta_t + c \sin \theta_t \cos V_e (a \sin \phi_t \sin V_r + b \cos \phi_t \cos V_r) \\ &- \frac{abc}{R_t} = 0 \quad . \quad (9) \end{aligned}$$

Provided that one has obtained a diffraction point  $(V_e, V_r)$  for a receiver location  $(R_t, \theta_t, \phi_t)$ , a numerical technique can now be developed from Equations (7), (8), and (9) to solve for  $(V_e + \Delta V_e, V_r + \Delta V_r)$  associated with a new receiver location  $(R_t + \Delta R_t, \theta_t + \Delta \theta_t, \phi_t + \Delta \phi_t)$ . Assuming that the  $i^{\text{th}}$  set of  $(R_t, \theta_t, \phi_t, V_e, V_r)$  is first known to satisfy  $F_i = H_i = G_i = 0$ , or at least approximately so, the next set  $(R_t + \Delta R_t, \theta_t + \Delta \theta_t, \phi_t + \Delta \phi_t, V_e + \Delta V_e, V_r + \Delta V_r)$  is obtained by enforcing  $F_{i+1} = H_{i+1} = G_{i+1} = 0$ , such that

$$F_{i+1} = F_i + F_{V_e} \Delta V_e + F_{V_r} \Delta V_r + F_Y \Delta Y = 0 \quad ,$$

$$G_{i+1} = G_i + G_{V_e} \Delta V_e + G_{V_r} \Delta V_r + G_Y \Delta Y$$

$$+ G_{\theta_t} \Delta \theta_t + G_{\phi_t} \Delta \phi_t + G_{R_t} \Delta R_t = 0$$

and

$$H_{i+1} = H_i + H_{V_e} \Delta V_e + H_{V_r} \Delta V_r + H_{\theta_t} \Delta \theta_t$$

$$+ H_{\phi_t} \Delta \phi_t + H_{R_t} \Delta R_t = 0 \quad .$$

In matrix form, it is given by

$$\begin{bmatrix} F_{V_e} & F_{V_r} & F_Y \\ G_{V_e} & G_{V_r} & G_Y \\ H_{V_e} & H_{V_r} & 0 \end{bmatrix} \begin{bmatrix} \Delta V_e \\ \Delta V_r \\ \Delta Y \end{bmatrix} = \begin{bmatrix} -F_i \\ -G_i - G_{\theta_t} \Delta \theta_t - G_{\phi_t} \Delta \phi_t - G_{R_t} \Delta R_t \\ -H_i - H_{\theta_t} \Delta \theta_t - H_{\phi_t} \Delta \phi_t - H_{R_t} \Delta R_t \end{bmatrix} \quad . \quad (10)$$

Note that the partial derivations are given by the following:

$$F_{V_e} = -[c^2 \cos^2 V_e + (a^2 \cos^2 V_r + b^2 \sin^2 V_r) \sin^2 V_e]^{1/2} \cos(\gamma - \alpha)$$

$$F_{V_r} = (b^2 - a^2) \sin V_r \cos V_r \left\{ \frac{\cos^2 V_{e_s}}{(a_s^2 \cos^2 V_r + b_s^2 \sin^2 V_r + Z_s^2 \cot^4 V_{e_s})^{1/2}} \right. \\ \left. - \int_{V_{e_s}}^{V_e} \frac{\sin^2 V_e'}{[c^2 \cos^2 V_e' + (a^2 \cos^2 V_r + b^2 \sin^2 V_r) \sin^2 V_e']^{1/2}} dV_e' \right\} \cos(\gamma - \alpha) \\ + \frac{r_e \sin(\gamma - \alpha) [a_s^2 b_s^2 + Z_s^2 \cot^4 V_{e_s} (a_s^2 \sin^2 V_r + b_s^2 \cos^2 V_r)]^{1/2}}{a_s^2 \cos^2 V_r + b_s^2 \sin^2 V_r + Z_s^2 \cot^4 V_{e_s}}$$

$$F_\gamma = r_s \sin \gamma - r_e \sin(\gamma - \alpha)$$

$$G_{V_e} = \frac{Dab(a^2 \cos^2 V_r + b^2 \sin^2 V_r - c^2) \sin V_e \cos V_e \cos(\gamma - \alpha)}{[c^2 \cos^2 V_e + (a^2 \cos^2 V_r + b^2 \sin^2 V_r) \sin^2 V_e]^{1/2}} \\ - \frac{\sin^3 \theta_t (a \sin \theta_t \cos V_r - b \cos \theta_t \sin V_r) [a^2 b^2 - (a^2 \sin^2 V_r + b^2 \cos^2 V_r) c^2] \sin V_e \cos V_e}{[(a^2 \sin^2 V_r + b^2 \cos^2 V_r) c^2 \cos^2 V_e + a^2 b^2 \sin^2 V_e]^{1/2}} \\ + \frac{abc \cos(\gamma - \alpha)}{D} [c^2 \cos^2 V_e + (a^2 \cos^2 V_r + b^2 \sin^2 V_r) \sin^2 V_e]^{1/2} . \\ \therefore \left\{ \frac{c^2 - (a^2 \cos^2 V_r + b^2 \sin^2 V_r)}{R_t^2} \sin V_e \cos V_e \right. \\ \left. + \sin^3 \theta_t \sin V_e \left( \frac{a}{R_t} \cos \theta_t \cos V_r + \frac{b}{R_t} \sin \theta_t \sin V_r \right) - \frac{c}{R_t} \cos^3 \theta_t \cos V_e \right\}$$

$$\begin{aligned}
G_{V_r} = & \frac{Dab \cos(\gamma-\alpha)(b^2-a^2)\sin V_r \cos V_r \sin^2 V_e}{[c^2 \cos^2 V_e + (a^2 \cos^2 V_r + b^2 \sin^2 V_r) \sin^2 V_e]^{1/2}} \\
& + Dab [c^2 \cos^2 V_e + (a^2 \cos^2 V_r + b^2 \sin^2 V_r) \sin^2 V_e]^{1/2} \sin(\gamma-\alpha) \cdot \\
& \cdot \frac{[a_s^2 h_s^2 + Z_s^2 \cot^4 V_{es} (a_s^2 \sin^2 V_r + b_s^2 \cos^2 V_r)]^{1/2}}{a_s^2 \cos^2 V_r + b_s^2 \sin^2 V_r + Z_s^2 \cot^4 V_{es}} \\
& + \frac{\sin \theta_t (a \sin \phi_t \cos V_r - b \cos \phi_t \sin V_r) (b^2 - a^2) \sin V_r \cos V_r c^2 \cos^2 V_e}{[(a^2 \sin^2 V_r + b^2 \cos^2 V_r) c^2 \cos^2 V_e + a^2 b^2 \sin^2 V_e]^{1/2}} \\
& + \sin \theta_t (a \sin \phi_t \sin V_r + b \cos \phi_t \cos V_r) [(a^2 \sin^2 V_r + b^2 \cos^2 V_r) \cdot \\
& \cdot c^2 \cos^2 V_e + a^2 b^2 \sin^2 V_e]^{1/2} \\
& + \frac{abc \cos(\gamma-\alpha)}{D} [c^2 \cos^2 V_e + (a^2 \cos^2 V_r + b^2 \sin^2 V_r) \sin^2 V_e]^{1/2} \cdot \\
& \cdot \left[ \frac{(b^2 - a^2)}{R_t^2} \sin V_r \cos V_r \cos^2 V_e - \sin \theta_t \cos V_e \left( \frac{b}{R_t} \sin \phi_t \cos V_r \right. \right. \\
& \left. \left. - \frac{a}{R_t} \cos \phi_t \sin V_r \right) \right]
\end{aligned}$$

$$G_r = -Dab \sin(\gamma-\alpha) [c^2 \cos^2 V_e + (a^2 \cos^2 V_r + b^2 \sin^2 V_r) \sin^2 V_e]^{1/2}$$

$$G_{\theta_t} = - \cos \theta_t (a \sin \phi_t \cos V_r - b \cos \phi_t \sin V_r) \cdot$$

$$\cdot [(a^2 \sin^2 V_r + b^2 \cos^2 V_r) c^2 \cos^2 V_e + a^2 b^2 \sin^2 V_e]^{1/2}$$

$$+ \frac{ab \cos(\gamma - \alpha)}{D} [c^2 \cos^2 V_e + (a^2 \cos^2 V_r + b^2 \sin^2 V_r) \sin^2 V_e]^{1/2} \cdot$$

$$\cdot \left\{ \frac{c}{R_t} \sin \theta_t \sin V_e - \cos \theta_t \cos V_e \left( \frac{a}{R_t} \cos \phi_t \cos V_r + \frac{b}{R_t} \sin \phi_t \sin V_r \right) \right\}$$

$$G_{\phi_t} = - \sin \theta_t (a \cos \phi_t \cos V_r + b \sin \phi_t \sin V_r) \cdot$$

$$\cdot [(a^2 \sin^2 V_r + b^2 \cos^2 V_r) c^2 \cos^2 V_e + a^2 b^2 \sin^2 V_e]^{1/2}$$

$$+ \frac{ab \cos(\gamma - \alpha)}{D} [c^2 \cos^2 V_e + (a^2 \cos^2 V_r + b^2 \sin^2 V_r) \sin^2 V_e]^{1/2} \cdot$$

$$\cdot \left\{ \sin \theta_t \cos V_e \left( \frac{a}{R_t} \sin \phi_t \cos V_r - \frac{b}{R_t} \cos \phi_t \sin V_r \right) \right\}$$

$$G_{R_t} = \frac{ab}{D} \cos(\gamma - \alpha) [c^2 \cos^2 V_e + (a^2 \cos^2 V_r + b^2 \sin^2 V_r) \sin^2 V_e]^{1/2} \cdot$$

$$\cdot \left\{ [\sin \theta_t \cos V_e (a \cos \phi_t \cos V_r + b \sin \phi_t \sin V_r) + c \cos \theta_t \sin V_e] / R_t^2 \right.$$

$$\left. - [\cos^2 V_e (a^2 \cos^2 V_r + b^2 \sin^2 V_r) + c^2 \sin^2 V_e] / R_t^3 \right\} \cdot$$

$$H_{V_e} = ab \cos V_e \cos \theta_t - c \sin V_e \sin \theta_t (a \sin \phi_t \sin V_r + b \cos \phi_t \cos V_r)$$

$$H_{V_r} = c \cos V_e \sin \theta_t (a \sin \phi_t \cos V_r - b \cos \phi_t \sin V_r)$$

$$H_Y = 0$$

$$H_\theta = -ab \sin V_e \sin \theta_t + c \cos V_e \cos \theta_t (a \sin \phi_t \sin V_r + b \cos \phi_t \cos V_r)$$

$$H_{\phi_t} = c \cos V_e \sin \theta_t (a \cos \phi_t \sin V_r - b \sin \phi_t \cos V_r)$$

and

$$H_{R_t} = \frac{abc}{R_t^2}.$$

It is seen that one can solve for  $(\Delta V_e, \Delta V_r, \Delta Y)$ , for a known  $(\Delta R_t, \Delta \theta_t, \Delta \phi_t)$ , using Equation (10). To obtain a diffraction point  $(V_e, V_r)$  for a given receiver location  $(R_t, \theta_t, \phi_t)$ , one can always assume the first diffraction point is at the source  $(V_e, V_r) = (V_{e_s}, V_{r_s})$  with the radiation direction  $(\theta_f, \phi_f = \frac{\pi}{2})$  for the positive ray (in  $\hat{Y}$  direction) or  $(\theta_f, \phi_f = \frac{3\pi}{2})$  for negative ray (in  $-\hat{Y}$  direction), and gradually add the increments  $(\Delta R_t, \Delta \theta_t, \Delta \phi_t)$  until the final radiation direction  $(\theta_t, \phi_t)$  is reached as shown in Figure 3. More detail on this topic is provided in Reference [4]. One need not start out from the source everytime, but obtains the new diffraction point directly from Equation (10), provided that the new receiver location does not deviate greatly from the previous direction.

After the geodesic path is determined, various other parameters associated with actual field calculation must be found. The Fock parameter  $r$  was calculated in Reference [2] as follows:

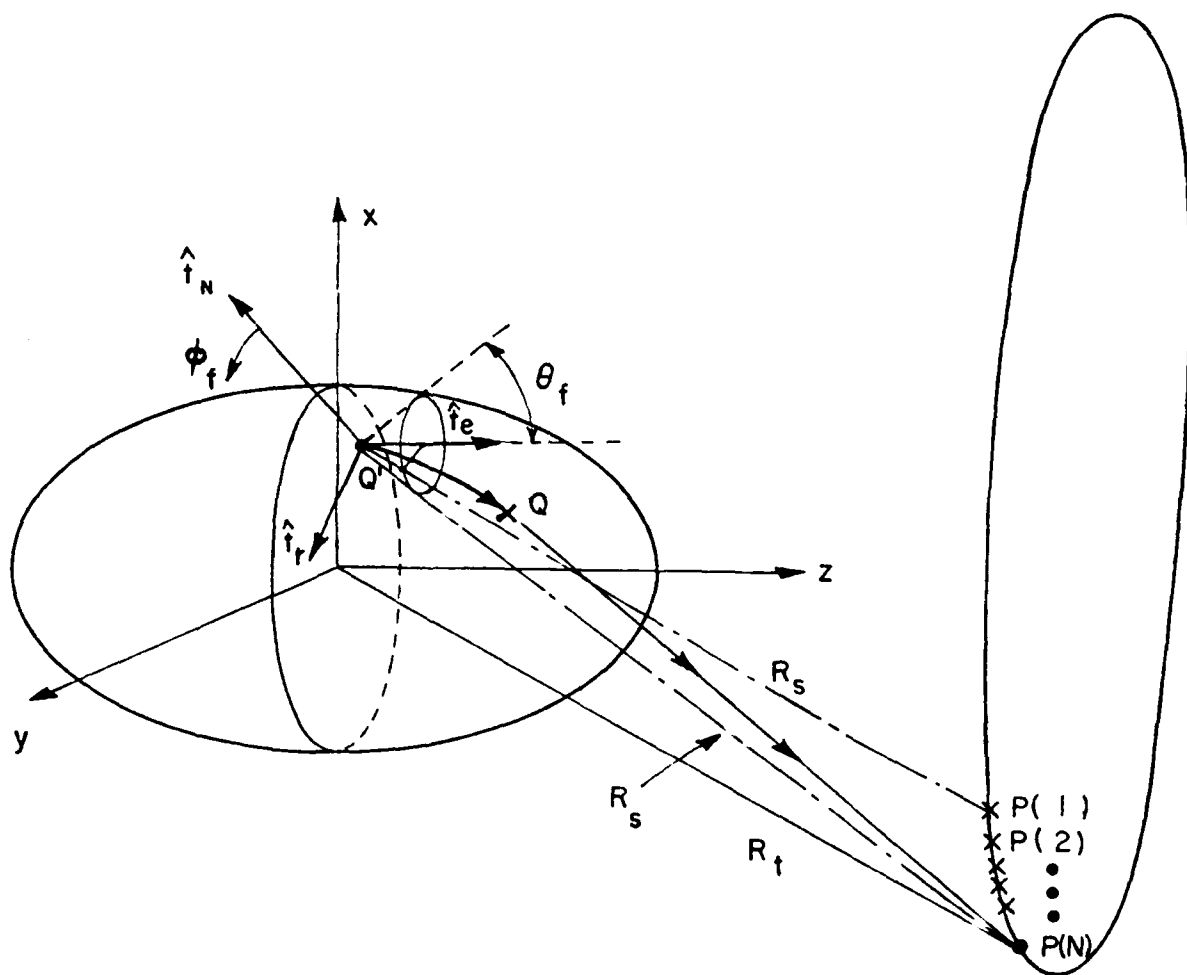


Figure 3. Illustration of the diffraction point finding for a given receiver location.



$$r = r_s \cos \gamma \left( \frac{V_r}{V_{rs}} \right) \frac{1}{\rho_g} \left( \frac{k \rho_g}{2} \right)^{1/3} \frac{1}{\cos^2(\gamma - \alpha)} \frac{d\alpha}{dV_r} dV_r'$$

where

$$\frac{d\alpha}{dV_r} = \frac{[a_s^2 b_s^2 + Z_s^2 \cot^4 V_{es} (a_s^2 \sin^2 V_r' + b_s^2 \cos^2 V_r')]^{1/2}}{a_s^2 \cos^2 V_r' + b_s^2 \sin^2 V_r' + Z_s^2 \cot^4 V_{es}}$$

or

$$r = \left( \frac{V_s}{V_{es}} \right) \frac{1}{\rho_g} \left( \frac{k \rho_g}{2} \right)^{1/3} \frac{1}{\sin(\gamma - \alpha)} \frac{dS_e}{dV_e'} dV_e'$$

Note that  $\rho_g = \frac{1}{k_1 \cos^2 \beta + k_2 \sin^2 \beta}$  and  $k_1$  and  $k_2$  are two principal curvatures.

Next, the ray divergence factor  $\sqrt{\frac{d\psi_0(Q')}{d\psi(Q')}}$  is defined as the change in the separation of adjacent surface rays as shown in Figure 4. Since the ellipsoid simulating the aircraft fuselage will be long and slender, it is assumed that the ray divergence factor is unity in the analysis.

This completes the elliptic cone perturbation solution for the antenna mounted on the off-mid section of an ellipsoid.

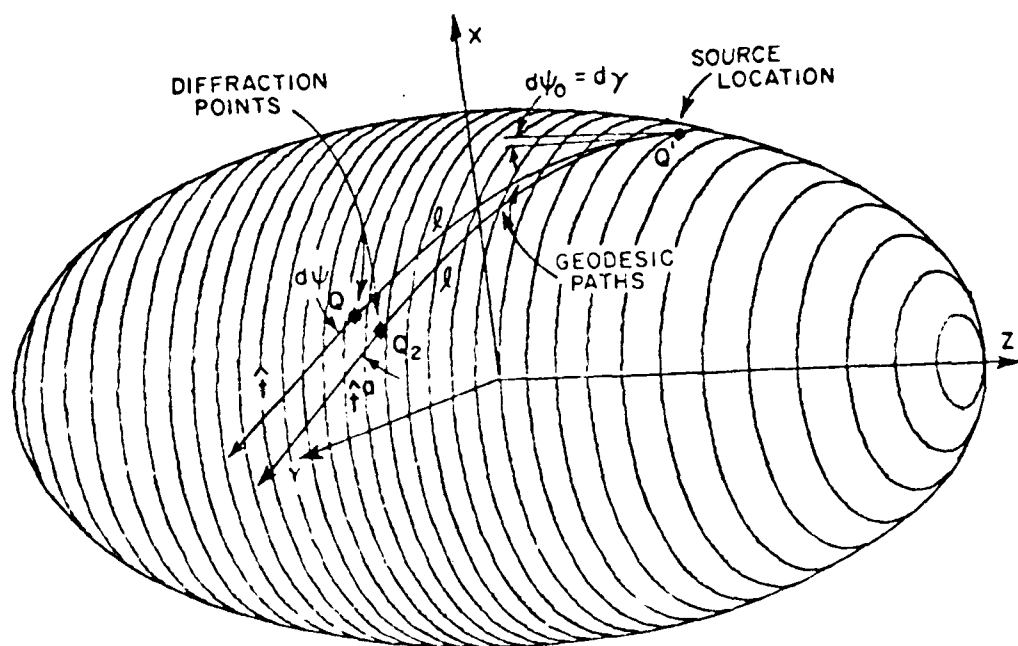


Figure 4. Illustration of the divergence factor  $(\sqrt{d\psi_0/d\psi})$  terms.

### III. RESULTS

The solutions presented in the previous chapter are employed to compute the near field radiation patterns for short monopoles or slots mounted on an ellipsoid.

To examine different conical pattern cuts, a cartesian coordinate system  $(x',y',z')$  originally defining the ellipsoid geometry is now rotated into a new system  $(x,y,z)$  as shown in Figure 5. Note that the new cartesian coordinates are found by first rotating about the  $z'$ -axis a angle  $\phi_C$  and then about the  $y$ -axis a angle  $\theta_C$ . The pattern is, then, taken in the  $(x,y,z)$  coordinate system with  $\theta_p$  fixed and  $\phi_p$  varied.

To show the validity of the elliptic cone perturbation solution, some typical sources, i.e., short monopole, axial slot and circumferential slot, and various source locations are chosen as shown in Figure 6.

For each case the following typical radiation patterns are obtained:

- a)  $\theta_C = 0^\circ$ ,  $\phi_C = 90^\circ$ ,  $\theta_p = 90^\circ$  (roll plane pattern)
- b)  $\theta_C = 30^\circ$ ,  $\phi_C = 90^\circ$ ,  $\theta_p = 90^\circ$
- c)  $\theta_C = 60^\circ$ ,  $\phi_C = 90^\circ$ ,  $\theta_p = 90^\circ$
- d)  $\theta_C = 90^\circ$ ,  $\phi_C = 90^\circ$ ,  $\theta_p = 90^\circ$  (elevation plane pattern)
- e)  $\theta_C = 90^\circ$ ,  $\phi_C = 0^\circ$ ,  $\theta_p = 90^\circ$  (azimuth plane pattern).

The radiation patterns obtained by the ellipsoid program, which uses an ellipsoid to simulate the aircraft fuselage, are compared to those obtained using the spheroid solution [5] in each case.

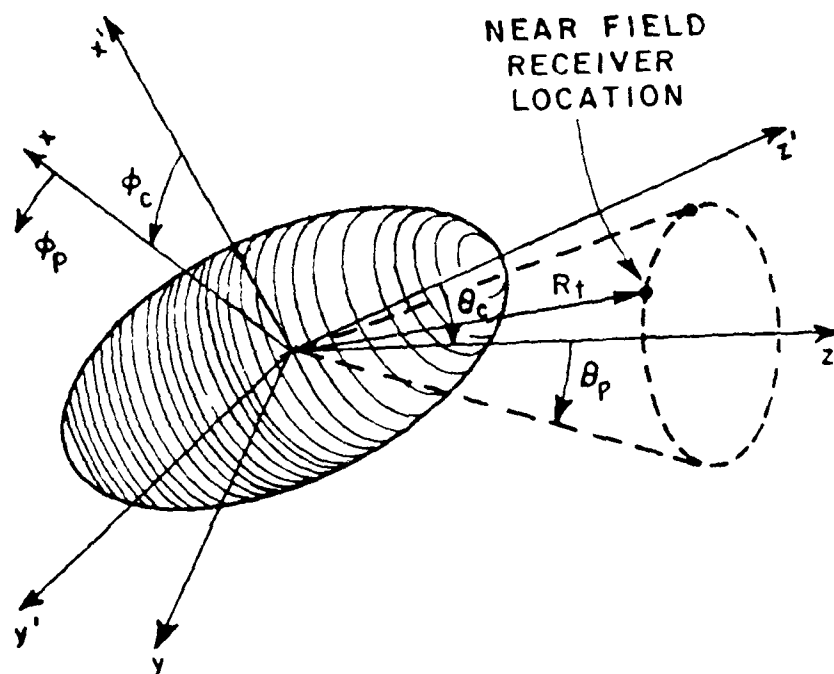


Figure 5. Definition of pattern axis.

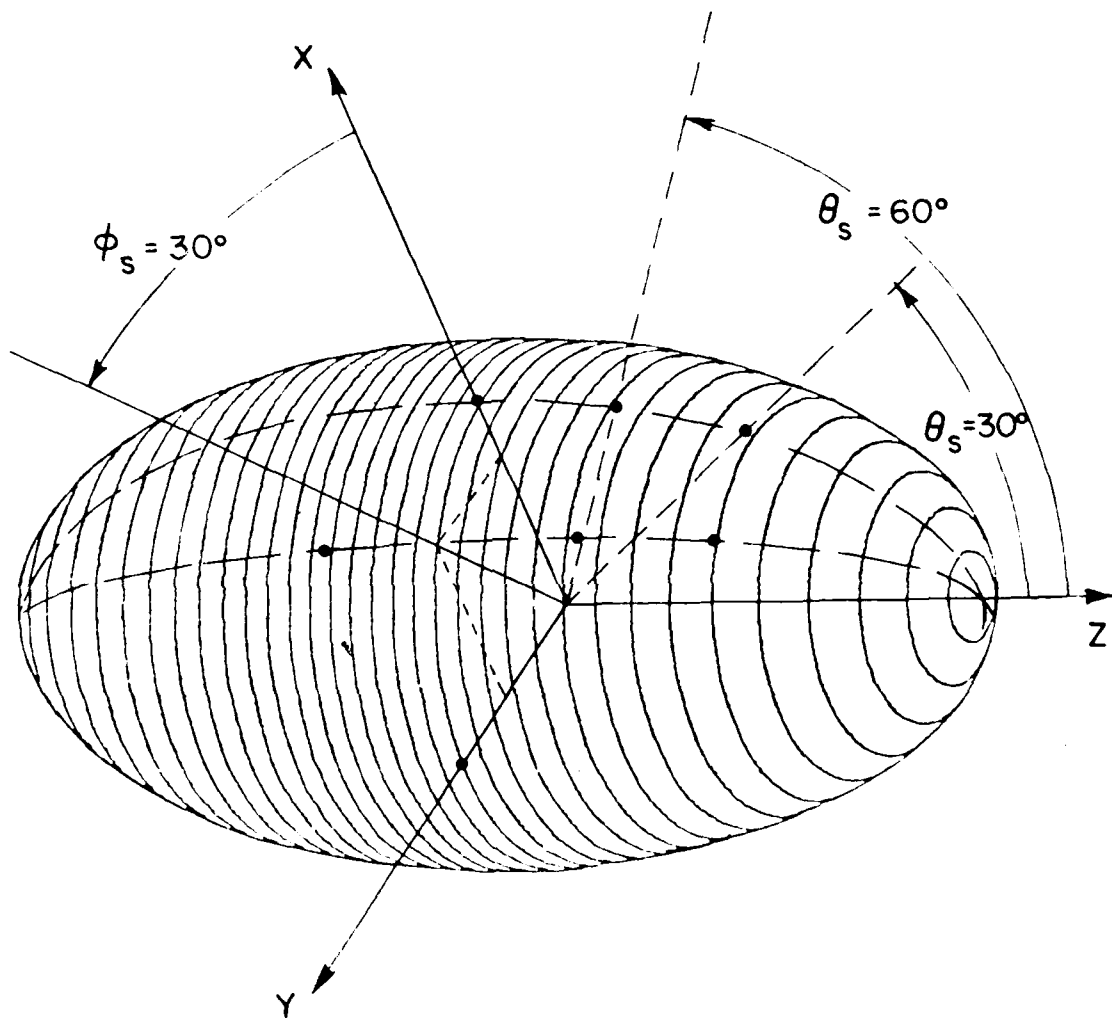


Figure 6. Various source locations tested.

It is noted that the geodesic tracing method of the ellipsoid program for the side mounted antennas (Figures 9, 10, 11, 14, 15, 18, 19) is different from that of the spheroid program because the ellipsoid is not a surface of revolution.

The exact agreement between the results of the ellipsoid program and the spheroid program as shown in Figures 7-19 gives one confidence about the validity of the elliptic cone technique.

Next, the ellipsoid program is employed to calculate the radiation patterns due to antennas mounted on an ellipsoid surface. The typical ellipsoid geometry ( $2\lambda \times 4\lambda \times 10\lambda$ ) is chosen and examined for various sources and source locations.

The cone boundary shown in Figure 32 is used in determining whether one or two rays are used in the solution. Note that  $\beta_{12}$  is defined automatically by determining the caustic angle in the elevation pattern ( $\beta_C$ ) and adding a few additional degrees to that value, i.e.,  $\beta_{12} = \beta_C + \Delta\beta$  where  $2^\circ < \Delta\beta < 10^\circ$ . One would expect to observe slight discontinuities somewhere, because various numbers of rays are included in different regions.

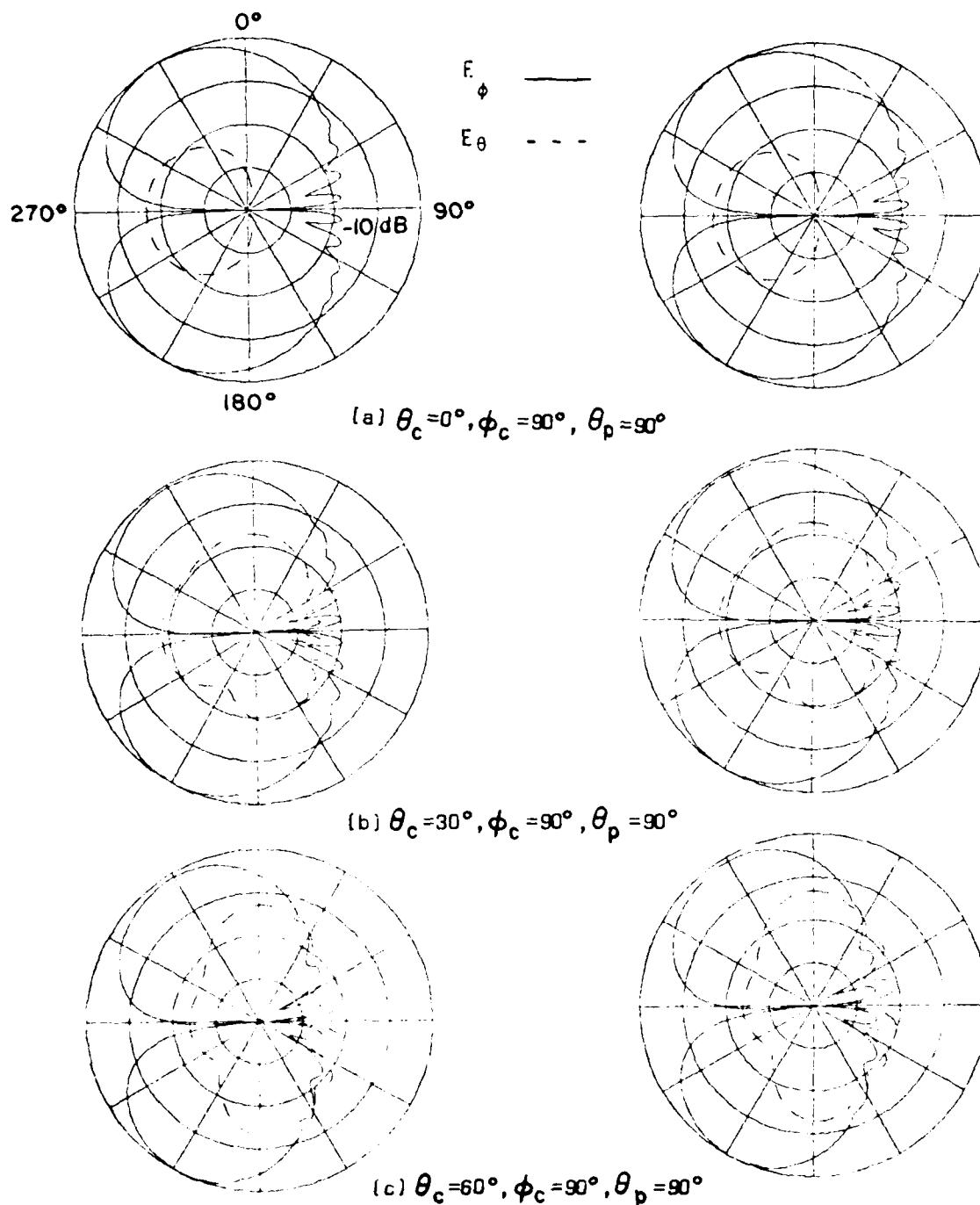
#### IV. CONCLUSIONS

The object of this study has been to develop an efficient numerical solution for the high frequency radiation patterns of an ellipsoid-mounted antenna. The UTD is used in this study to calculate the radiation patterns, and the elliptic cone perturbation method is applied

to simulate the geodesic paths on the ellipsoid, which in turn can be used to model an aircraft or missile fuselage. For a given radiation direction in the shadow region, the geodesic path and final diffraction point on the ellipsoid can, then, be found via an efficient numerical approach.

The exact agreement of the radiation patterns from two different programs confirms that this elliptic cone perturbation solution is very useful in predicting the high frequency radiation patterns for antennas mounted on the off-mid section of an ellipsoid.

This numerical solution will be employed, along with flat plates to construct a general solution for calculating radiation patterns due to airborne antennas.

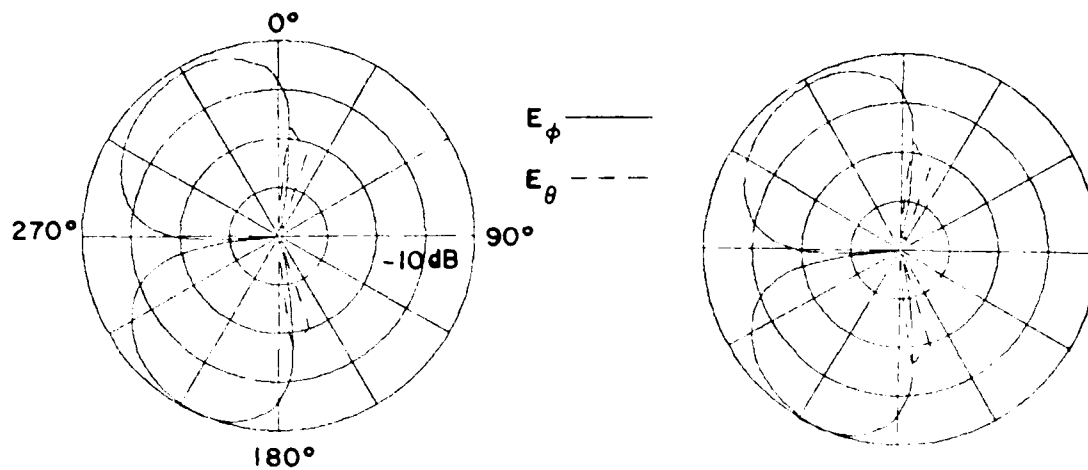


Ellipsoid Program

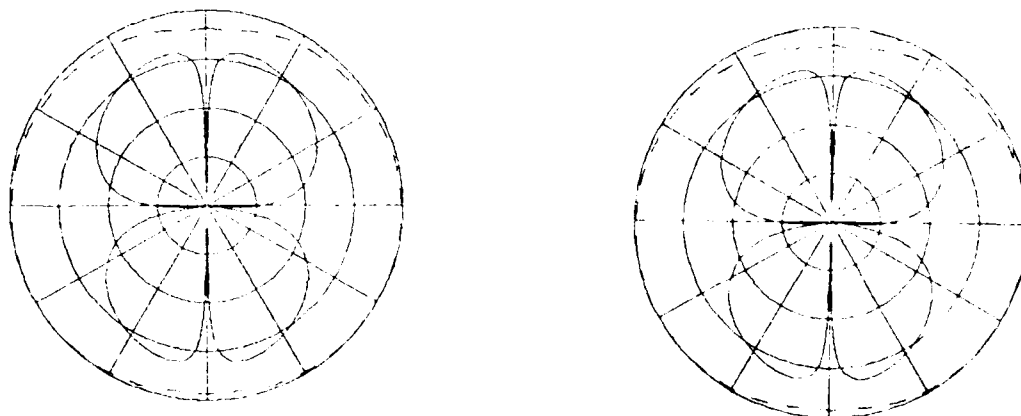
Spheroid Program

Figure 7. Comparison of radiation patterns for  $R_t = 15\lambda$  for a short monopole mounted at  $\phi_s = 0^\circ, \theta_s = 60^\circ$  on a  $2\lambda \times 10\lambda$  spheroid.





(d)  $\theta_c = 90^\circ, \phi_c = 90^\circ, \theta_p = 90^\circ$

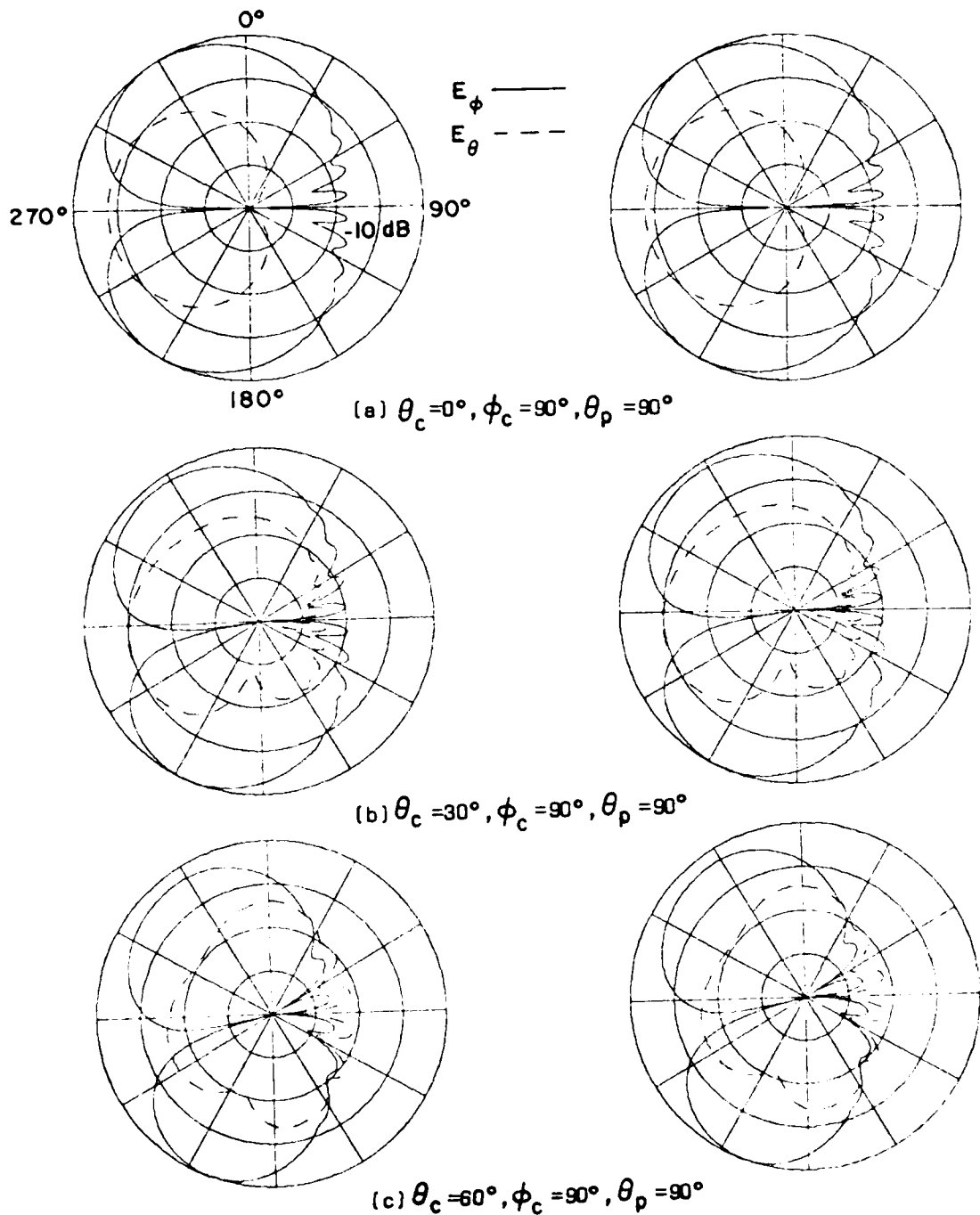


(e)  $\theta_c = 90^\circ, \phi_c = 0^\circ, \theta_p = 90^\circ$

Ellipsoid Program

Spheroid Program

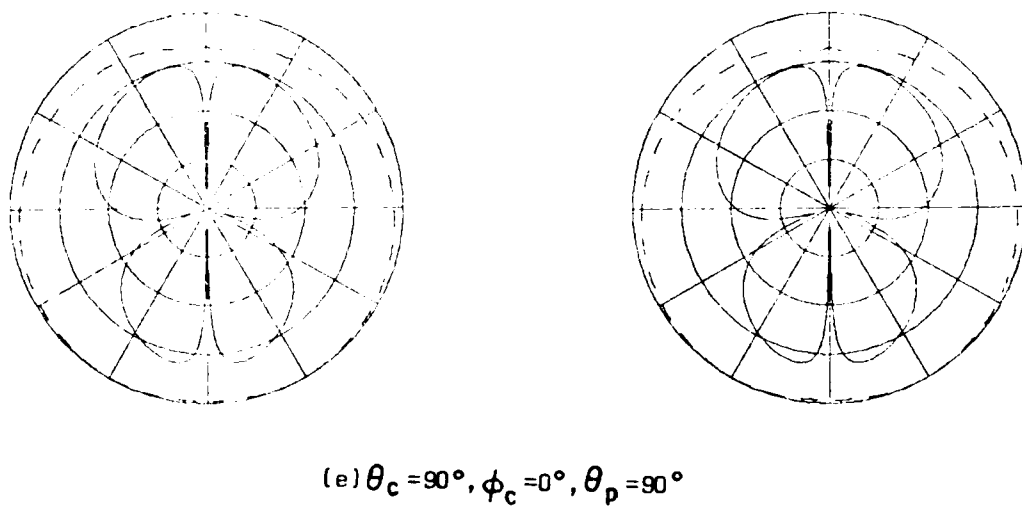
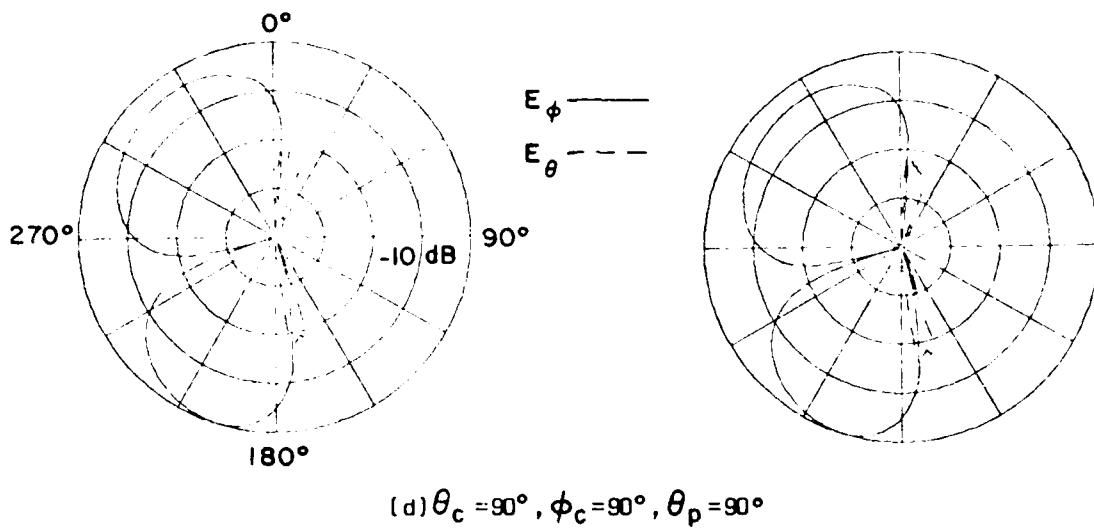
Figure 7. (continued)



Ellipsoid Program

Spheroid Program

Figure 8. Comparison of radiation patterns for a short monopole mounted at  $\phi_S = 0^\circ$ ,  $\theta_S = 30^\circ$  on a  $2\lambda \times 10\lambda$  spheroid.



Ellipsoid Program

Spheroid Program

Figure 8. (continued)

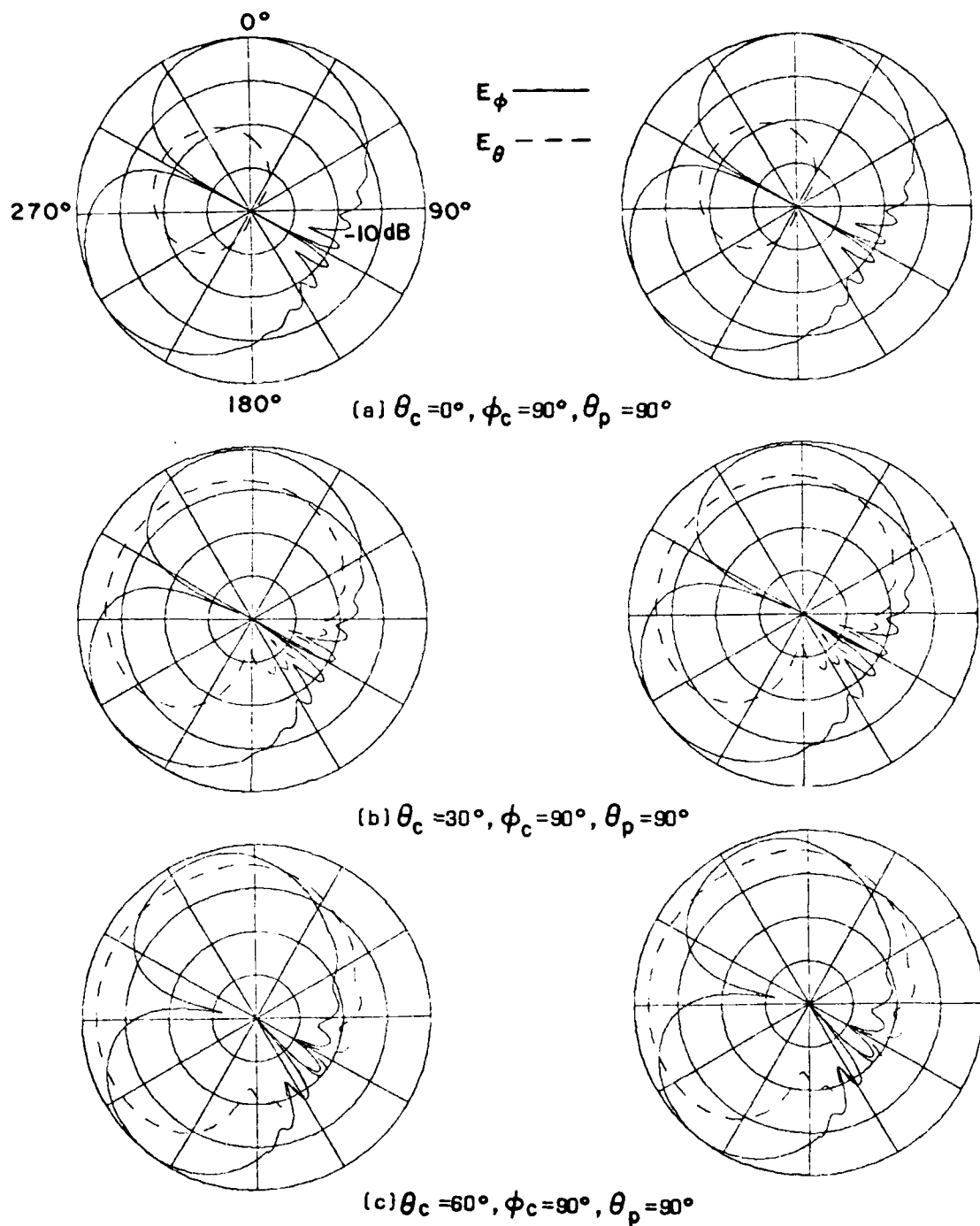
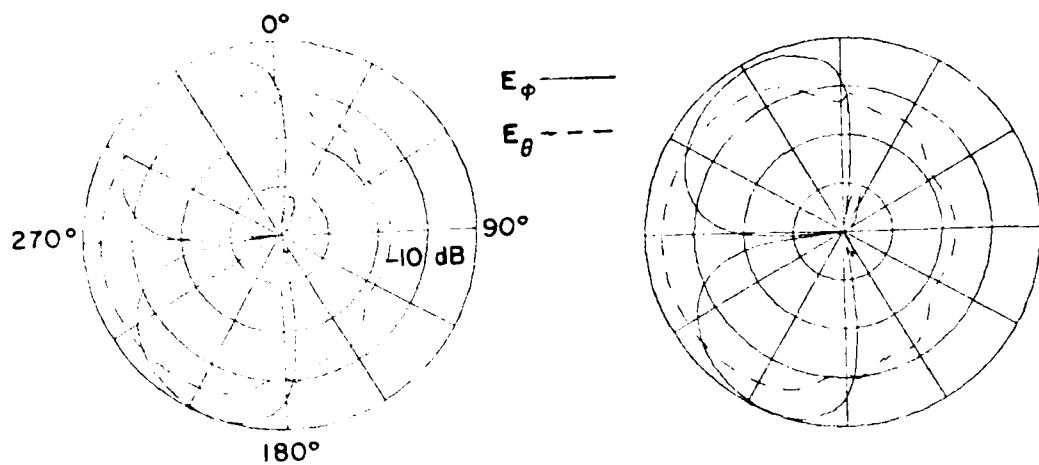
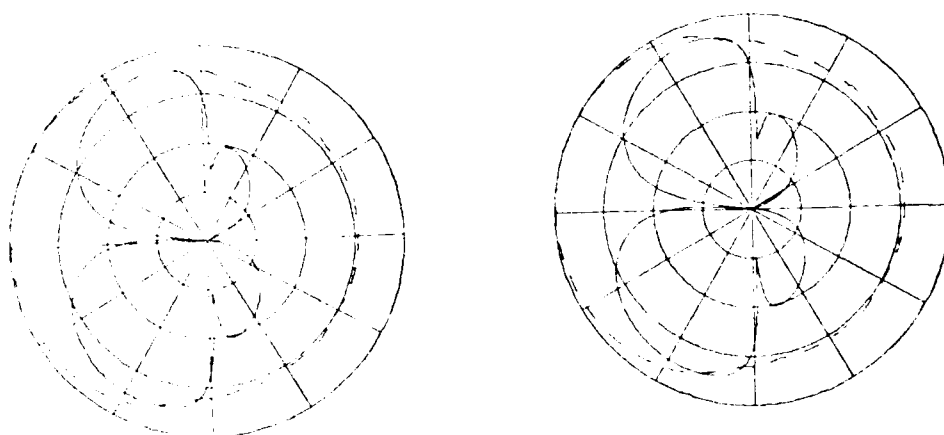


Figure 9. Comparison of radiation patterns for a short monopole mounted at  $\phi_s = 30^\circ, \theta_s = 60^\circ$  on a  $2\lambda \times 10\lambda$  spheroid.



(d)  $\theta_c = 90^\circ, \phi_c = 90^\circ, \theta_p = 90^\circ$

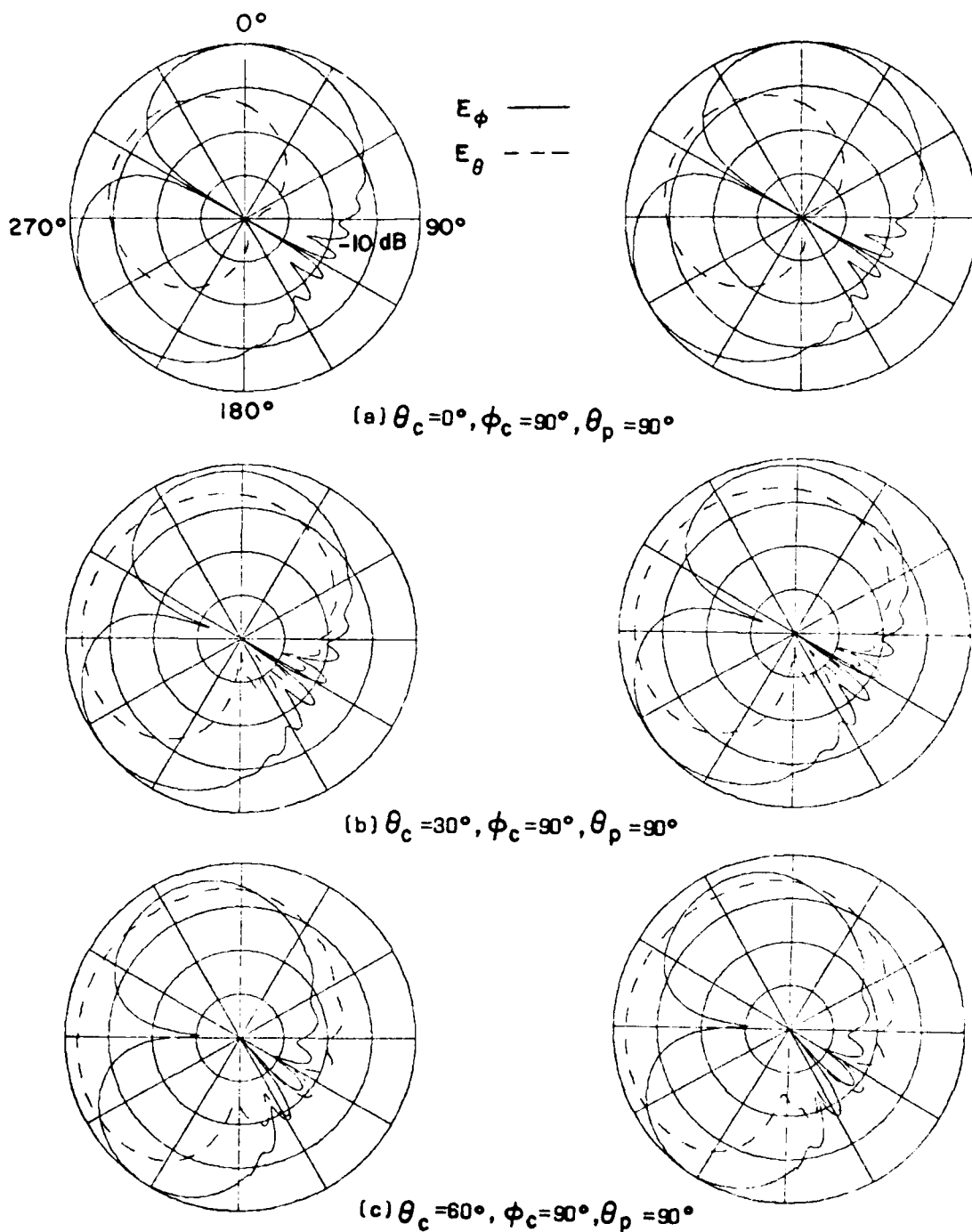


(e)  $\theta_c = 90^\circ, \phi_c = 0^\circ, \theta_p = 90^\circ$

Ellipsoid Program

Spheroid Program

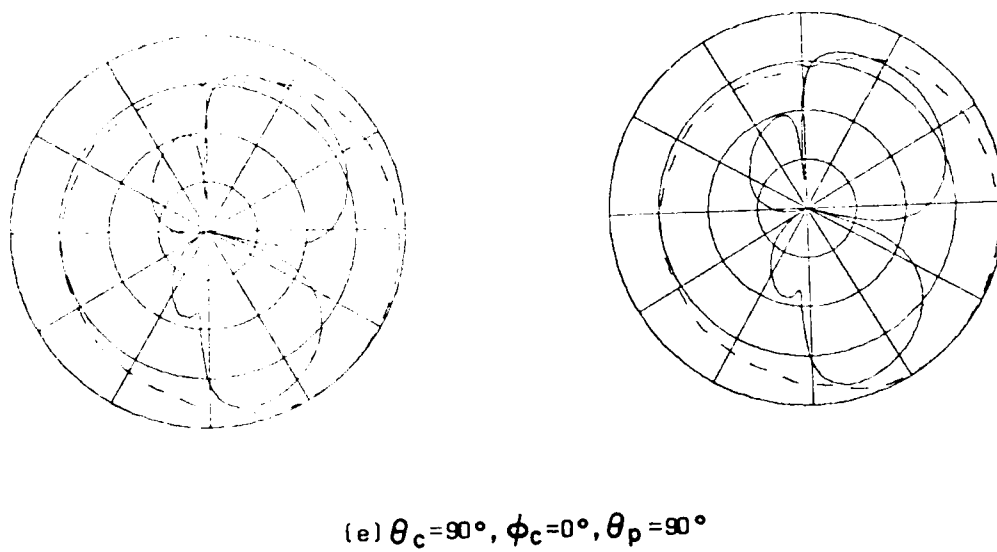
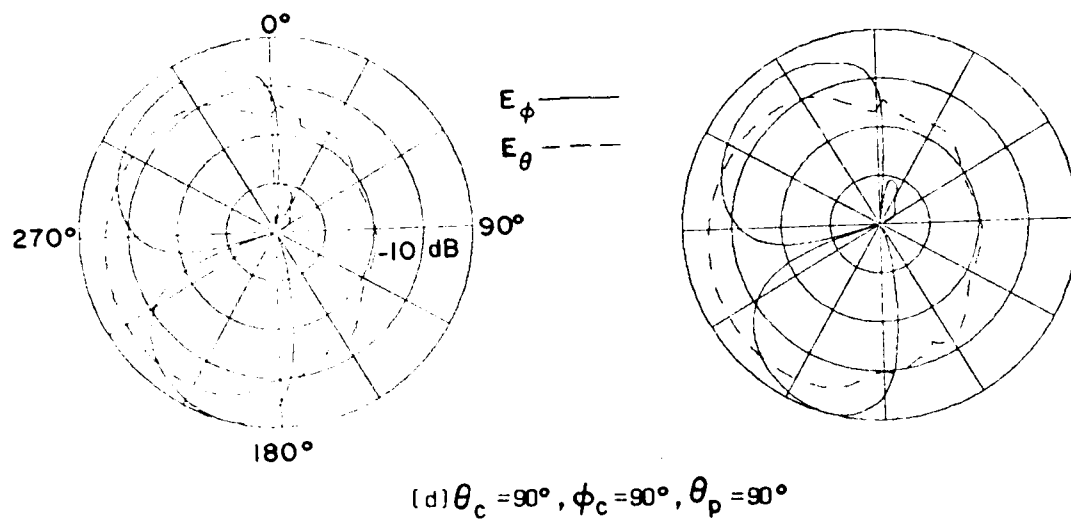
Figure 9. (continued)



Ellipsoid Program

Spheroid Program

Figure 10. Comparison of radiation patterns for a short monopole mounted at  $\phi_s = 30^\circ$ ,  $\theta_s = 30^\circ$  on a  $2\lambda \times 10\lambda$  spheroid.



Ellipsoid Program

Spheroid Program

Figure 10. (continued)

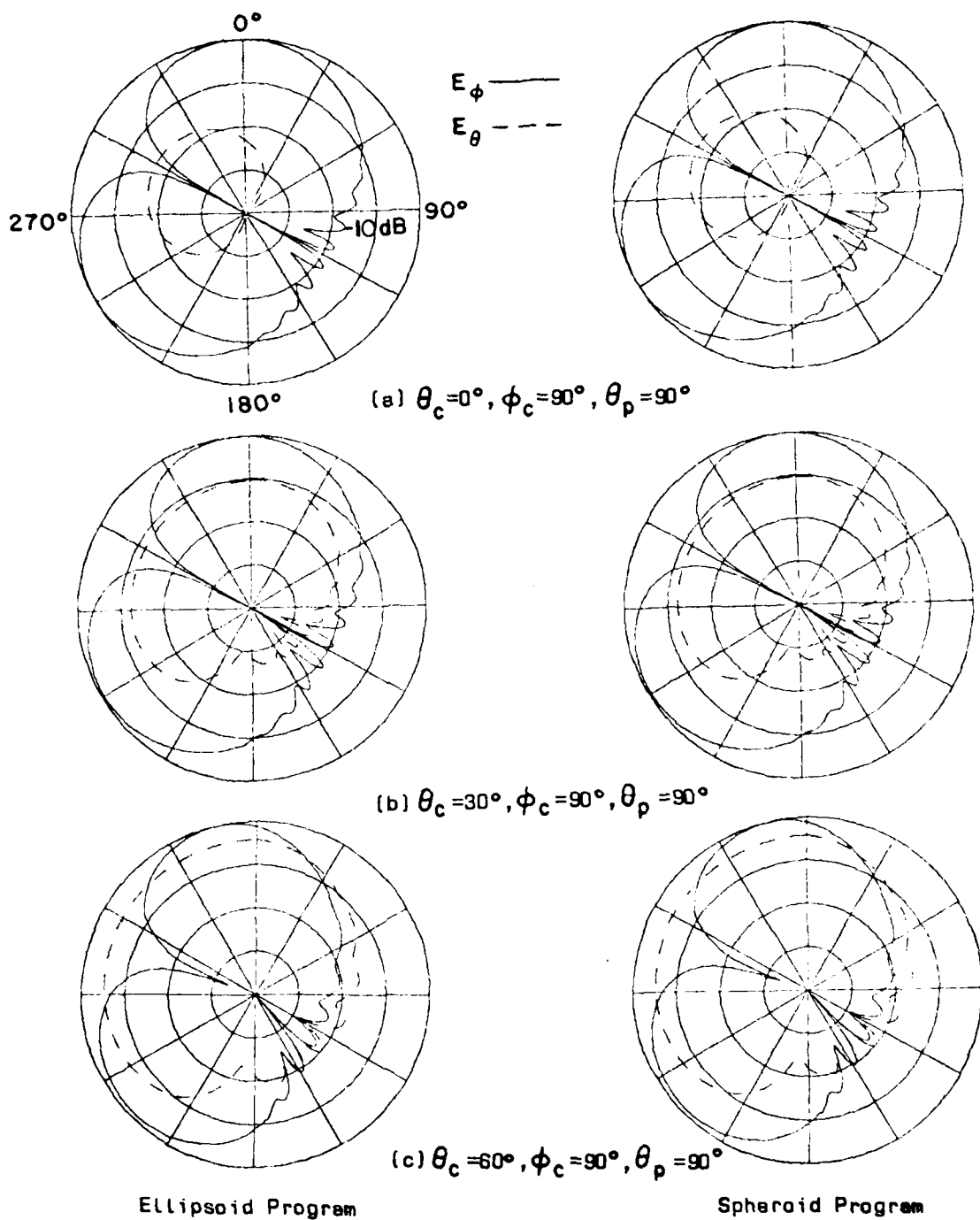
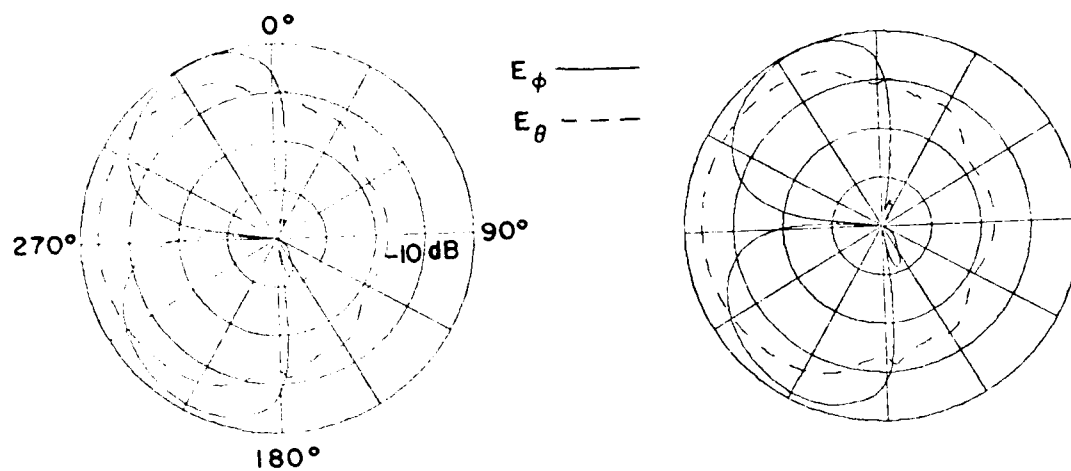
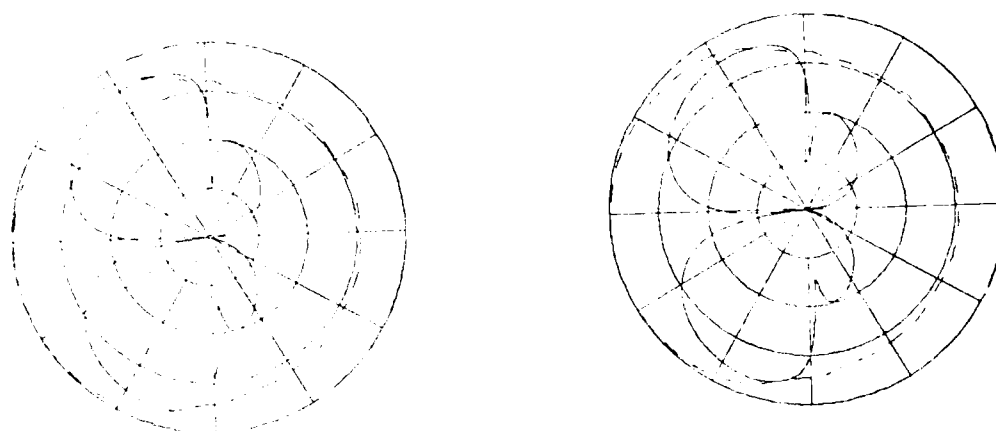


Figure 11. Comparison of radiation patterns for a short monopole mounted at  $\phi_s = 30^\circ$ ,  $\theta_s = 120^\circ$  on a  $2\lambda \times 10\lambda$  spheroid.





(d)  $\theta_c = 90^\circ, \phi_c = 90^\circ, \theta_p = 90^\circ$



(e)  $\theta_c = 90^\circ, \phi_c = 0^\circ, \theta_p = 90^\circ$

Ellipsoid Program

Spheroid Program

Figure 11. (continued)

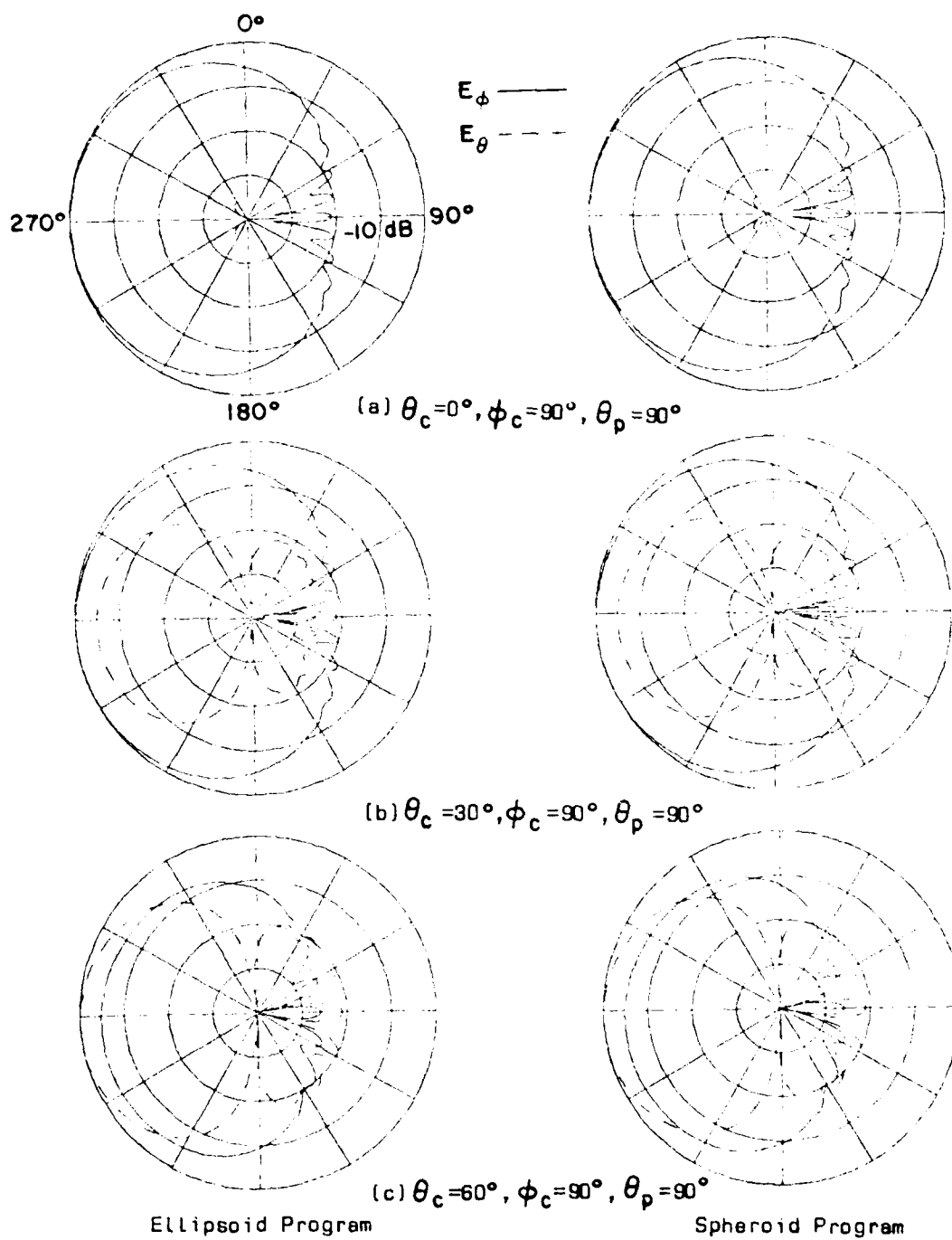
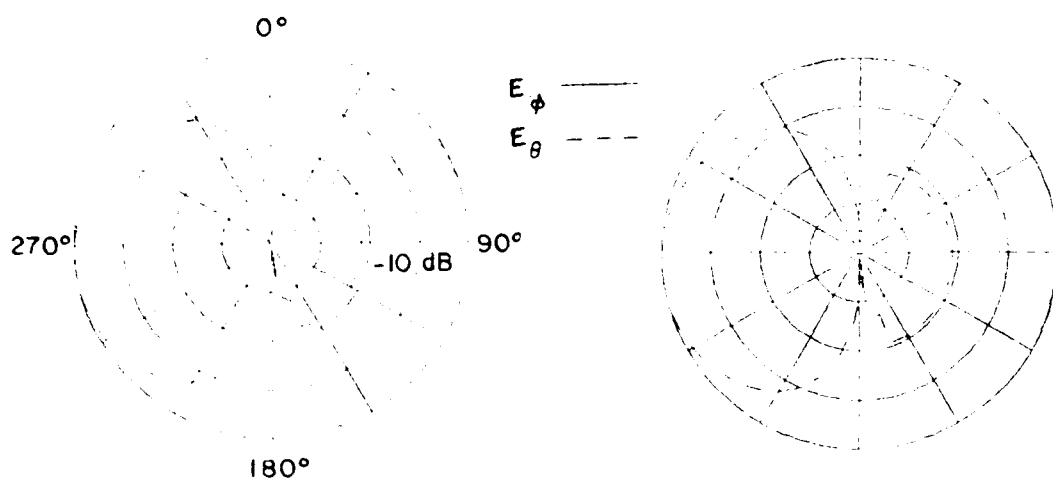
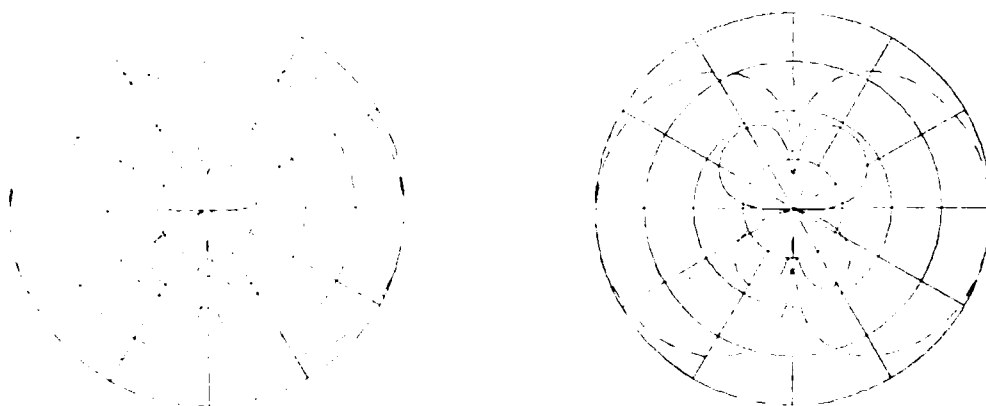


Figure 12. Comparison of radiation patterns for an axial slot mounted at  $\theta_s = 0^\circ, \theta_s = 60^\circ$  on a  $2\lambda \times 10\lambda$  spheroid.



(d)  $\theta_c = 90^\circ, \phi_c = 90^\circ, \theta_p = 90^\circ$



(e)  $\theta_c = 90^\circ, \phi_c = 0^\circ, \theta_p = 90^\circ$

Ellipsoid Program

Spheroid Program

Figure 12. (continued)

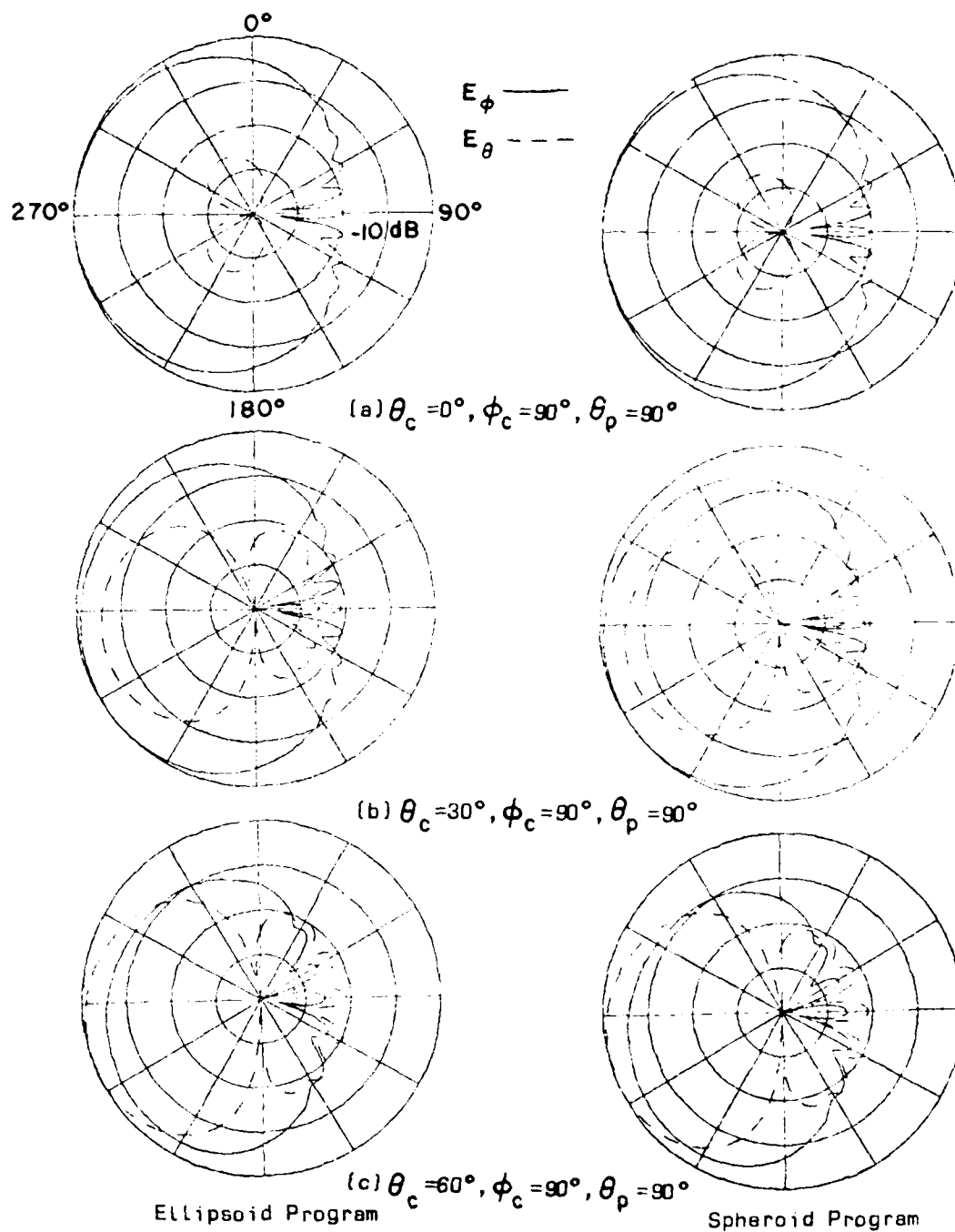
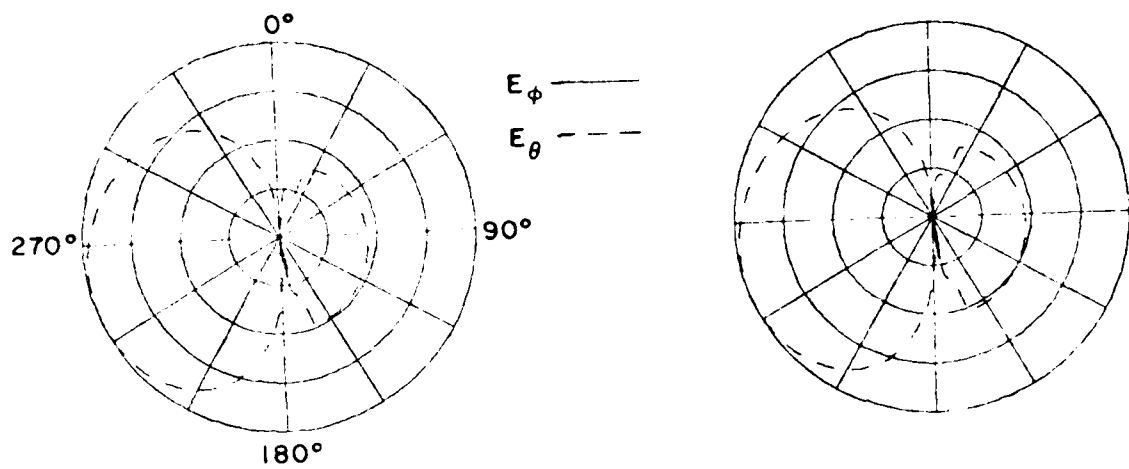
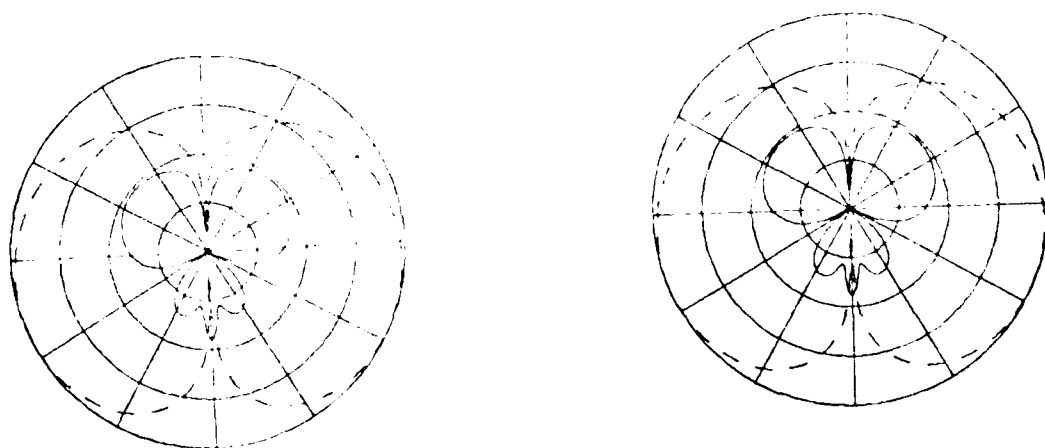


Figure 13. Comparison of radiation patterns for an axial slot mounted at  $\phi_s = 0^\circ$ ,  $\theta_s = 30^\circ$  on a  $2\lambda \times 10\lambda$  spheroid.



(d)  $\theta_c = 90^\circ, \phi_c = 90^\circ, \theta_p = 90^\circ$



(e)  $\theta_c = 90^\circ, \phi_c = 0^\circ, \theta_p = 90^\circ$

Ellipsoid Program

Spheroid Program

Figure 13. (continued)

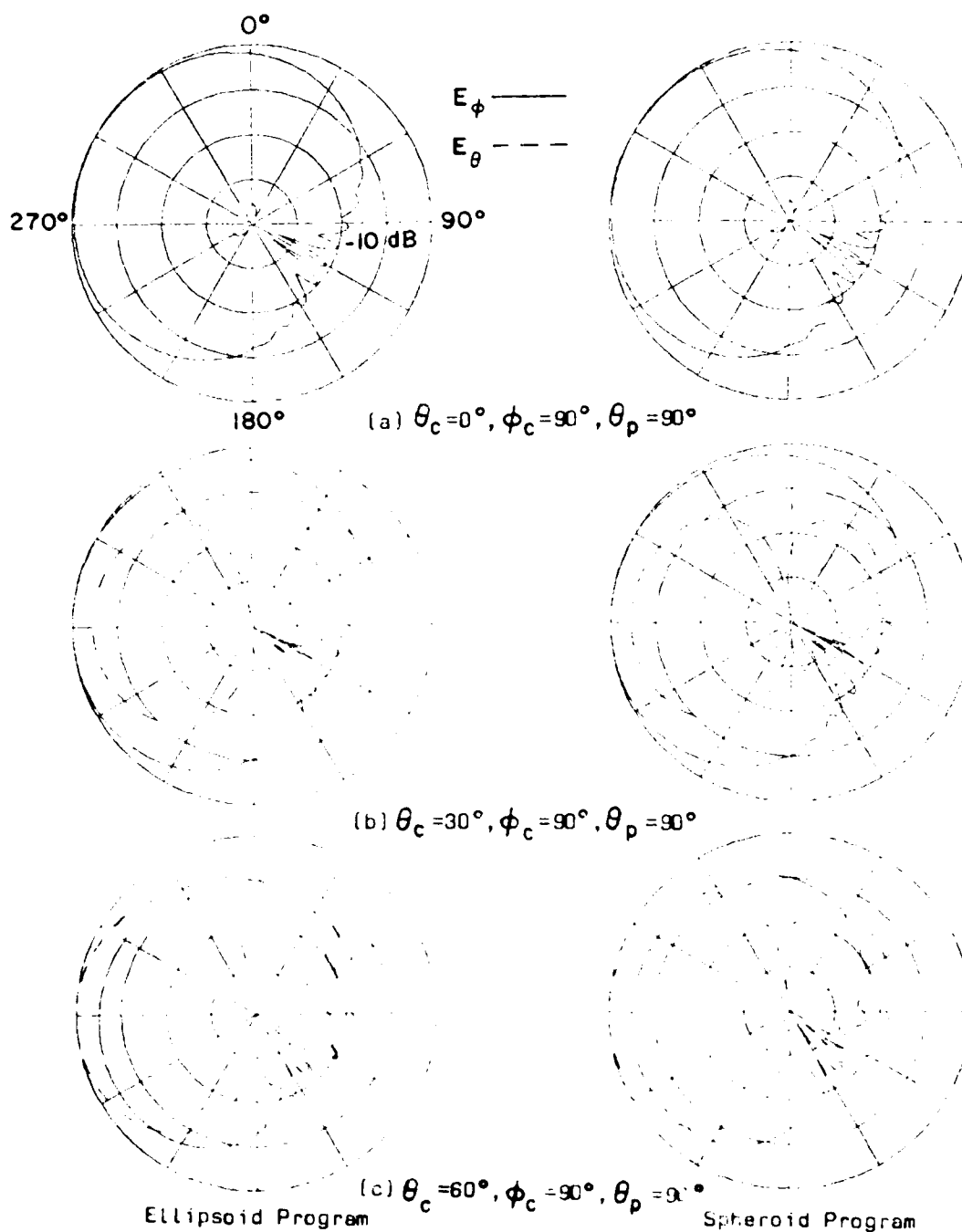
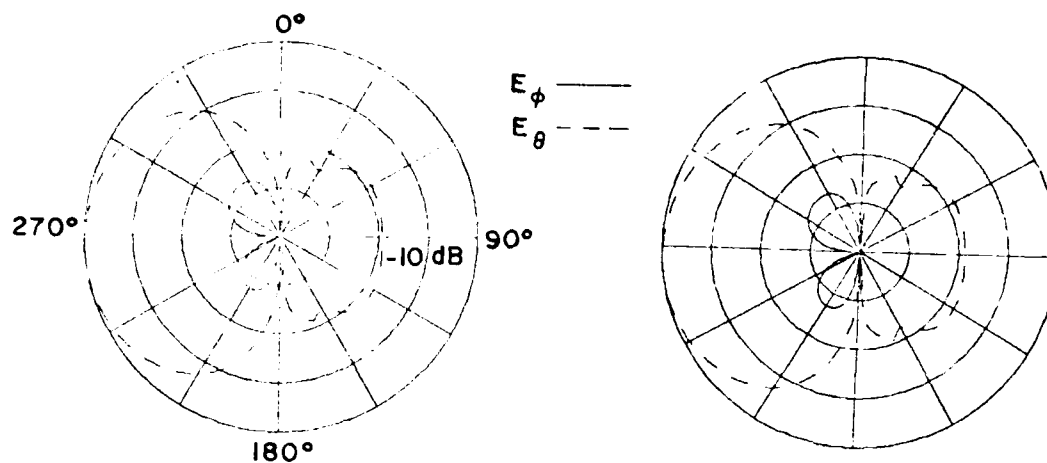
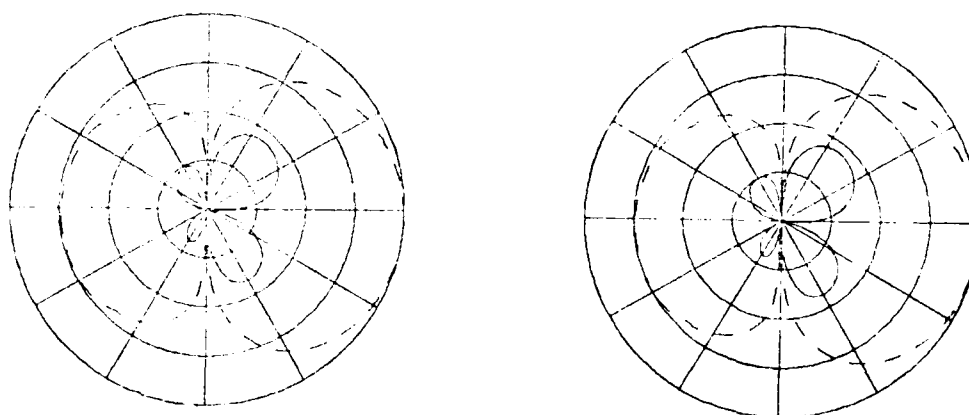


Figure 14. Comparison of radiation patterns for an axial slot mounted at  $\theta_s = 30^\circ$ ,  $\phi_s = 60^\circ$  on a  $2\lambda \times 10\lambda$  spheroid.



(d)  $\theta_c = 90^\circ, \phi_c = 90^\circ, \theta_p = 90^\circ$



(e)  $\theta_c = 90^\circ, \phi_c = 0^\circ, \theta_p = 90^\circ$

Ellipsoid Program

Spheroid Program

Figure 14. (continued)

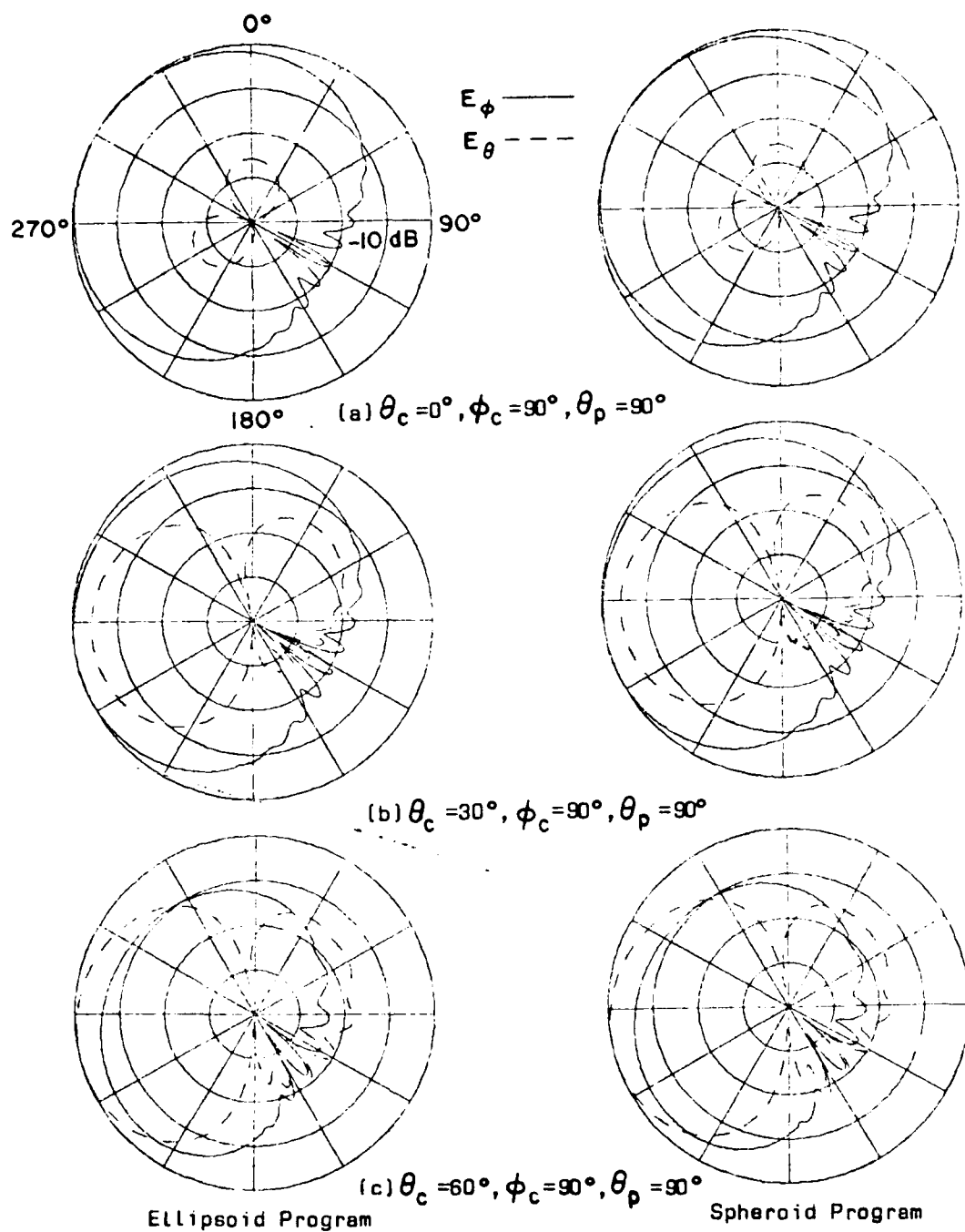
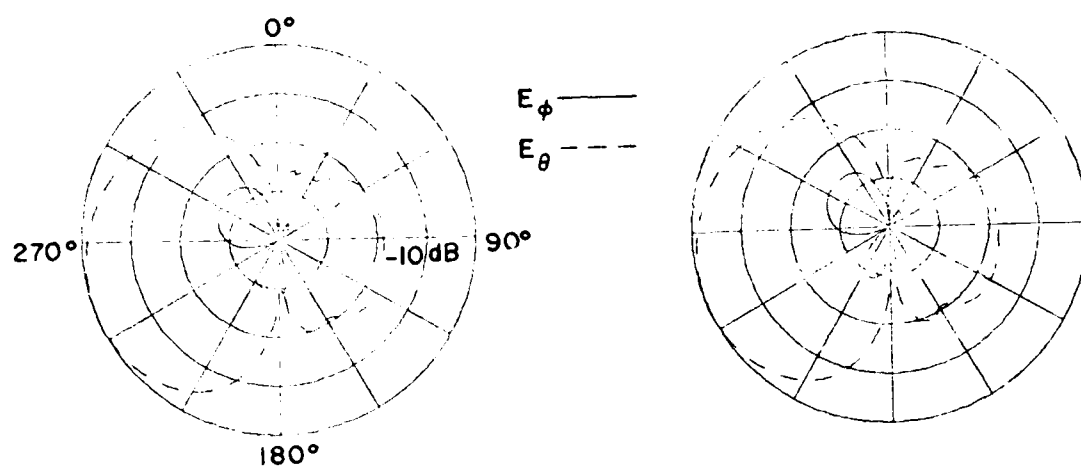
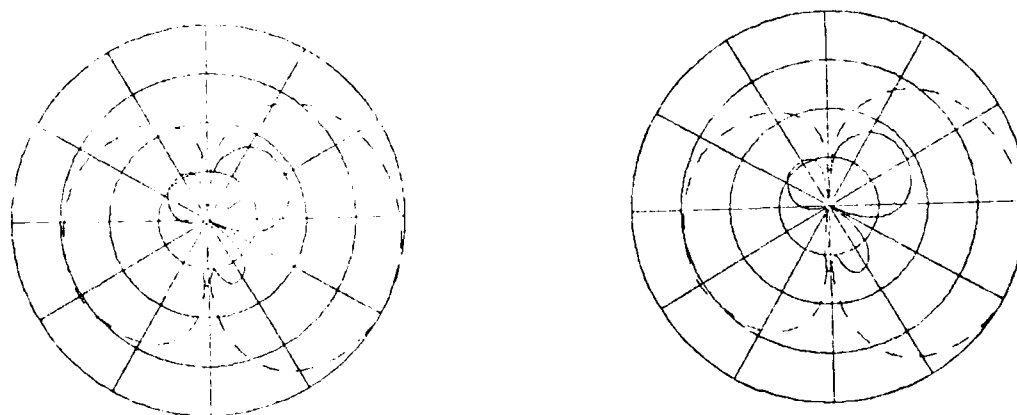


Figure 15. Comparison of radiation patterns for an axial slot mounted at  $\phi_s = 30^\circ$ ,  $\alpha_s = 30^\circ$  on a  $2\lambda \times 10\lambda$  spheroid.





(d)  $\theta_c = 90^\circ, \phi_c = 90^\circ, \theta_p = 90^\circ$



(e)  $\theta_c = 90^\circ, \phi_c = 0^\circ, \theta_p = 90^\circ$

Ellipsoid Program

Spheroid Program

Figure 15. (continued)

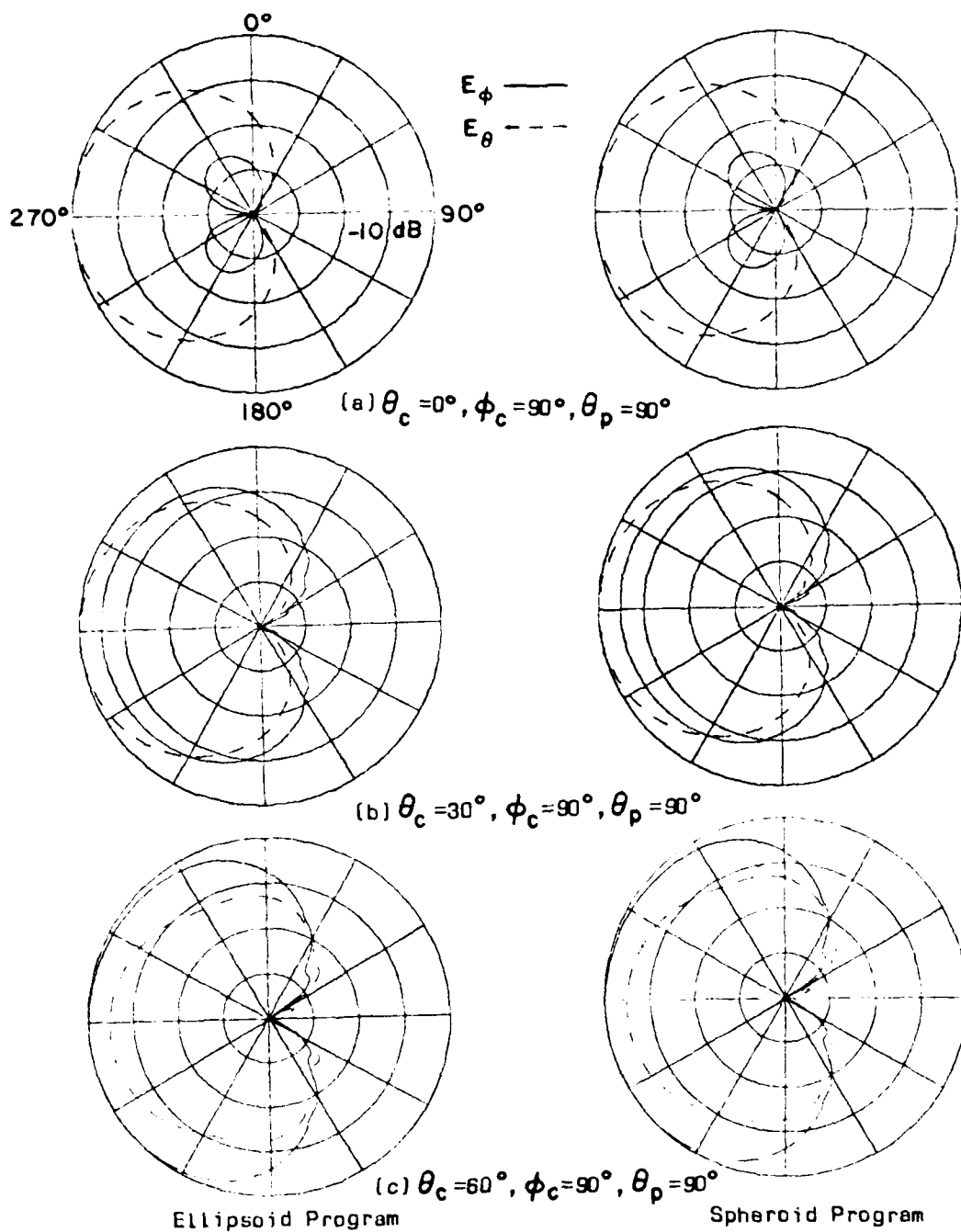
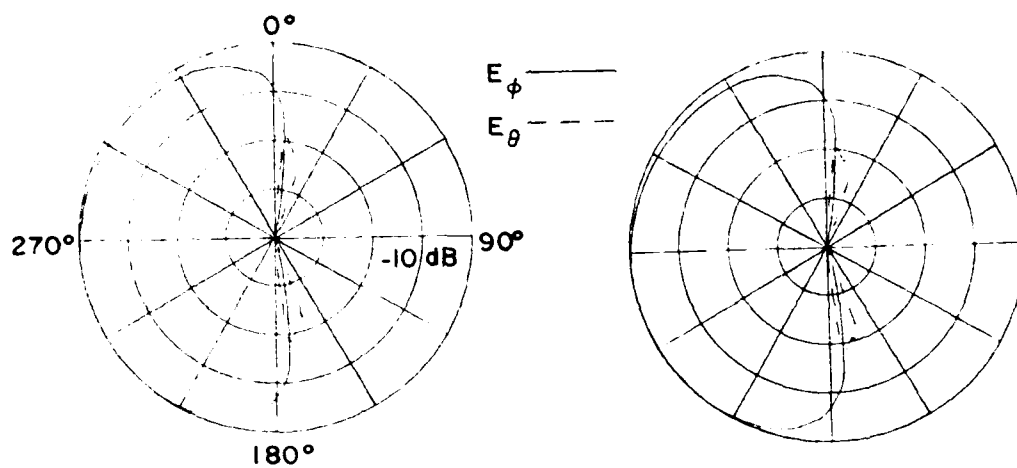
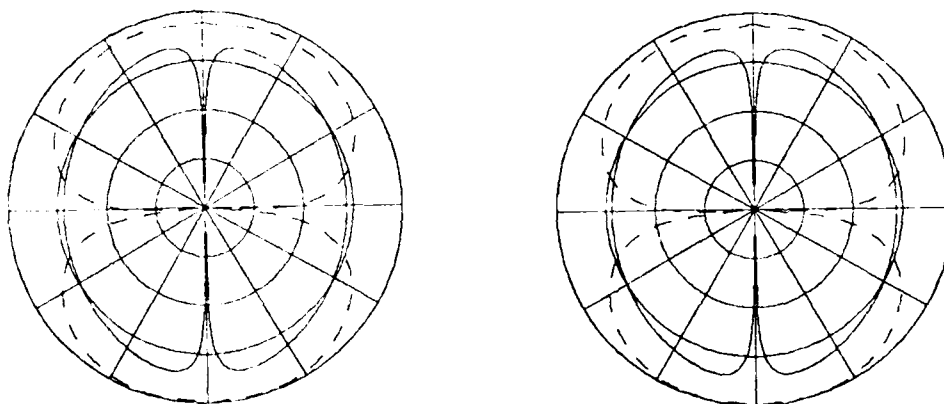


Figure 16. Comparison of radiation patterns for a circumferential slot mounted at  $\phi_s = 0^\circ, \theta_s = 60^\circ$  on a  $2\lambda \times 10\lambda$  spheroid.



(d)  $\theta_c = 90^\circ, \phi_c = 90^\circ, \theta_p = 90^\circ$



(e)  $\theta_c = 90^\circ, \phi_c = 0^\circ, \theta_p = 90^\circ$

Ellipsoid Program

Spheroid Program

Figure 16. (continued)

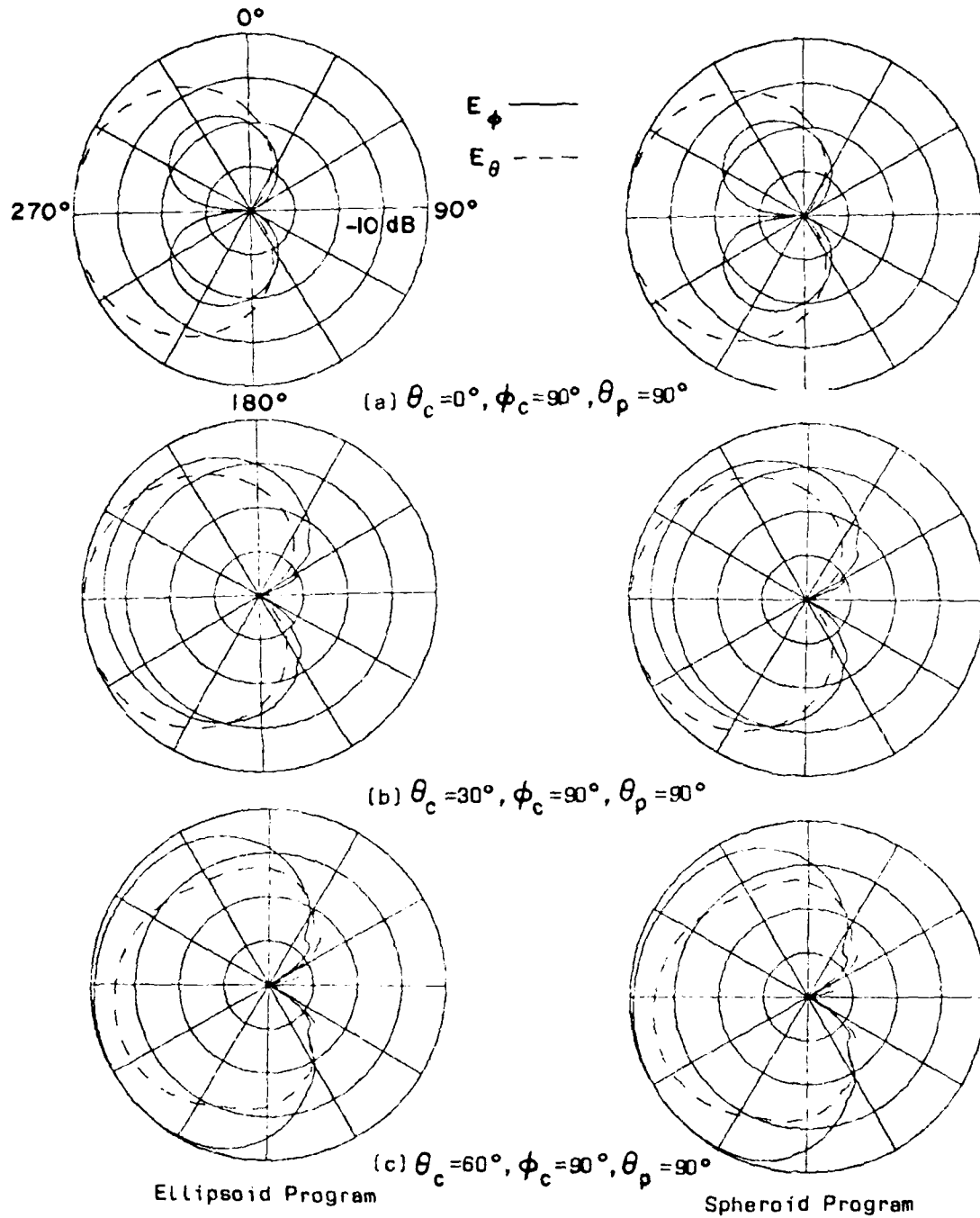
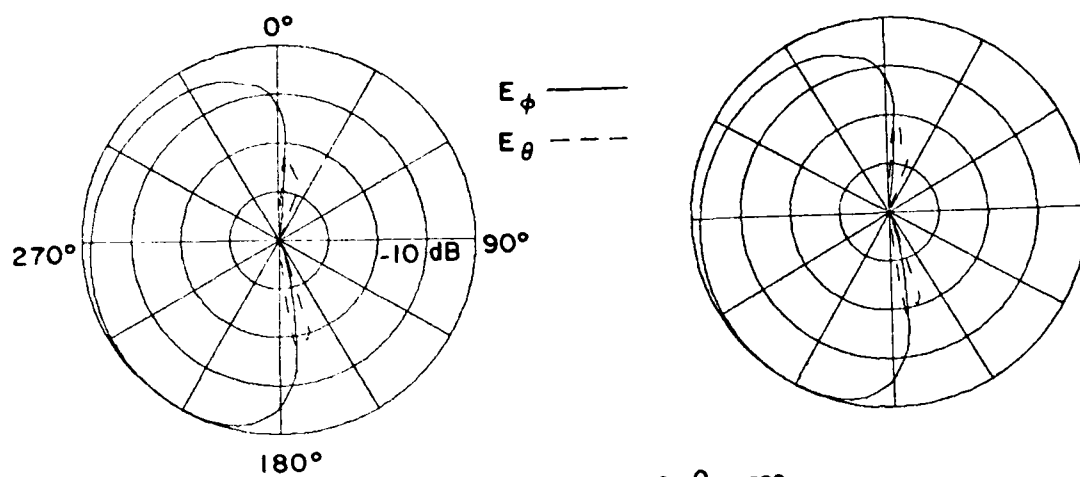
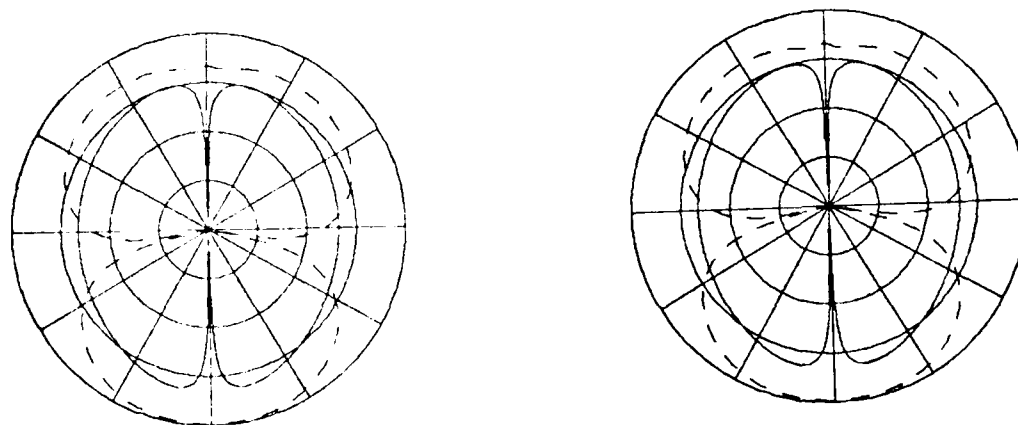


Figure 17. Comparison of radiation patterns for a circumferential slot mounted at  $\phi_s = 0^\circ$ ,  $\theta_s = 30^\circ$  on a  $2\lambda \times 10\lambda$  spheroid.



(d)  $\theta_c = 90^\circ, \phi_c = 90^\circ, \theta_p = 90^\circ$



(e)  $\theta_c = 90^\circ, \phi_c = 0^\circ, \theta_p = 90^\circ$

Ellipsoid Program

Spheroid Program

Figure 17. (continued)

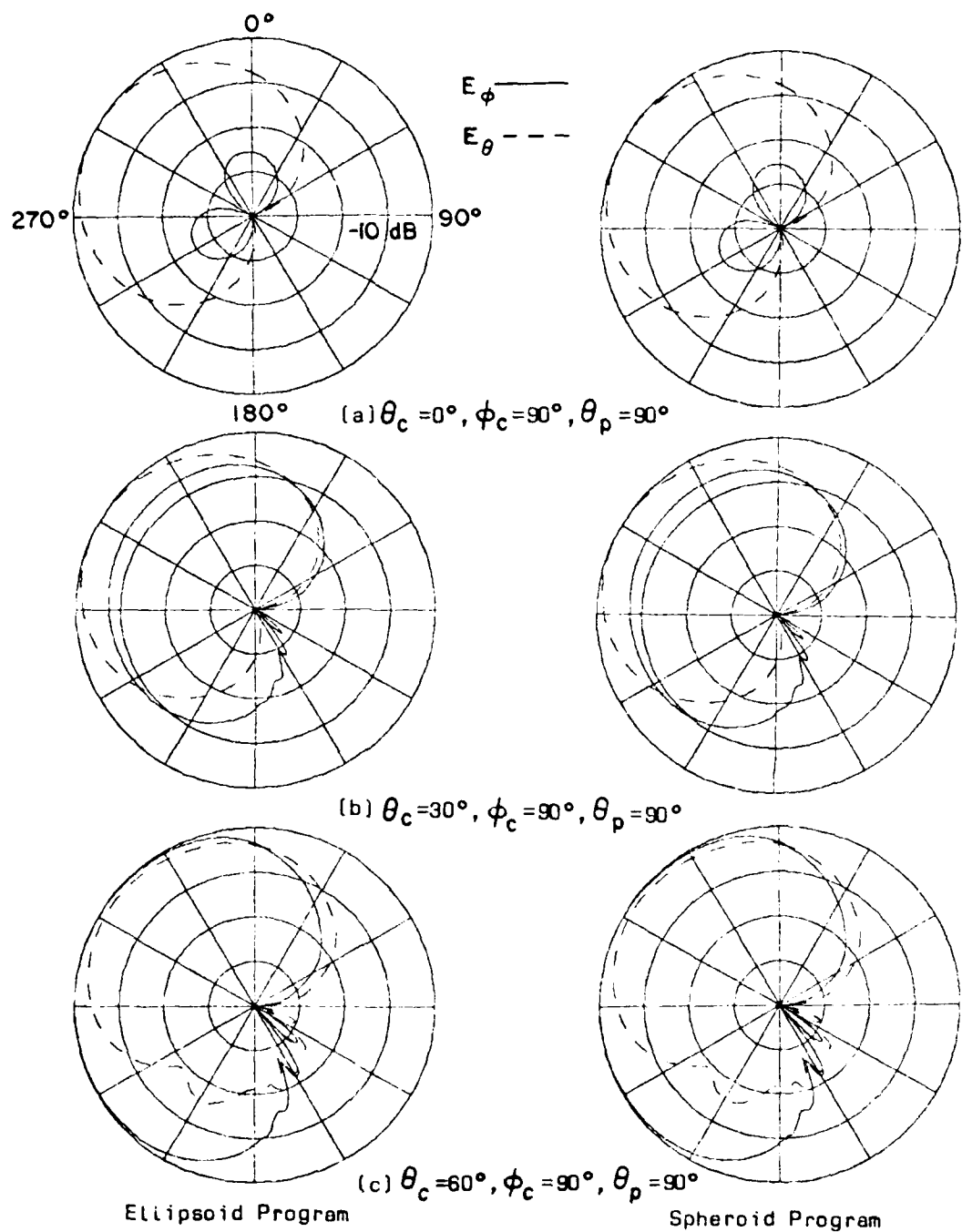
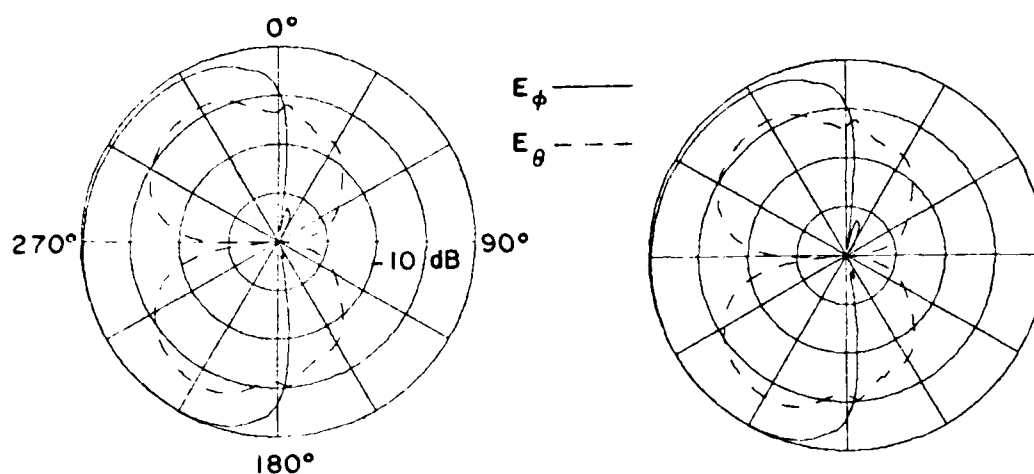
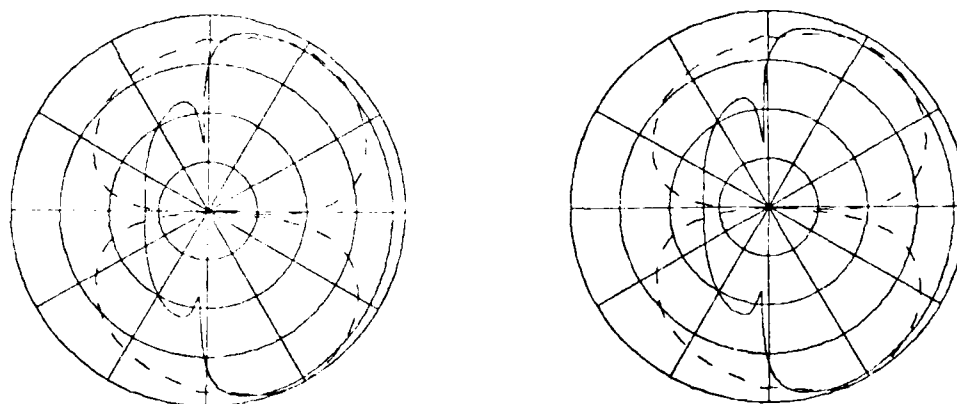


Figure 18. Comparison of radiation patterns for a circumferential slot mounted at  $\phi_s = 30^\circ, \theta_s = 60^\circ$  on a  $2\lambda \times 10\lambda$  spheroid.



(d)  $\theta_c = 90^\circ, \phi_c = 90^\circ, \theta_p = 90^\circ$



(e)  $\theta_c = 90^\circ, \phi_c = 0^\circ, \theta_p = 90^\circ$

Ellipsoid Program

Spheroid Program

Figure 18. (continued)

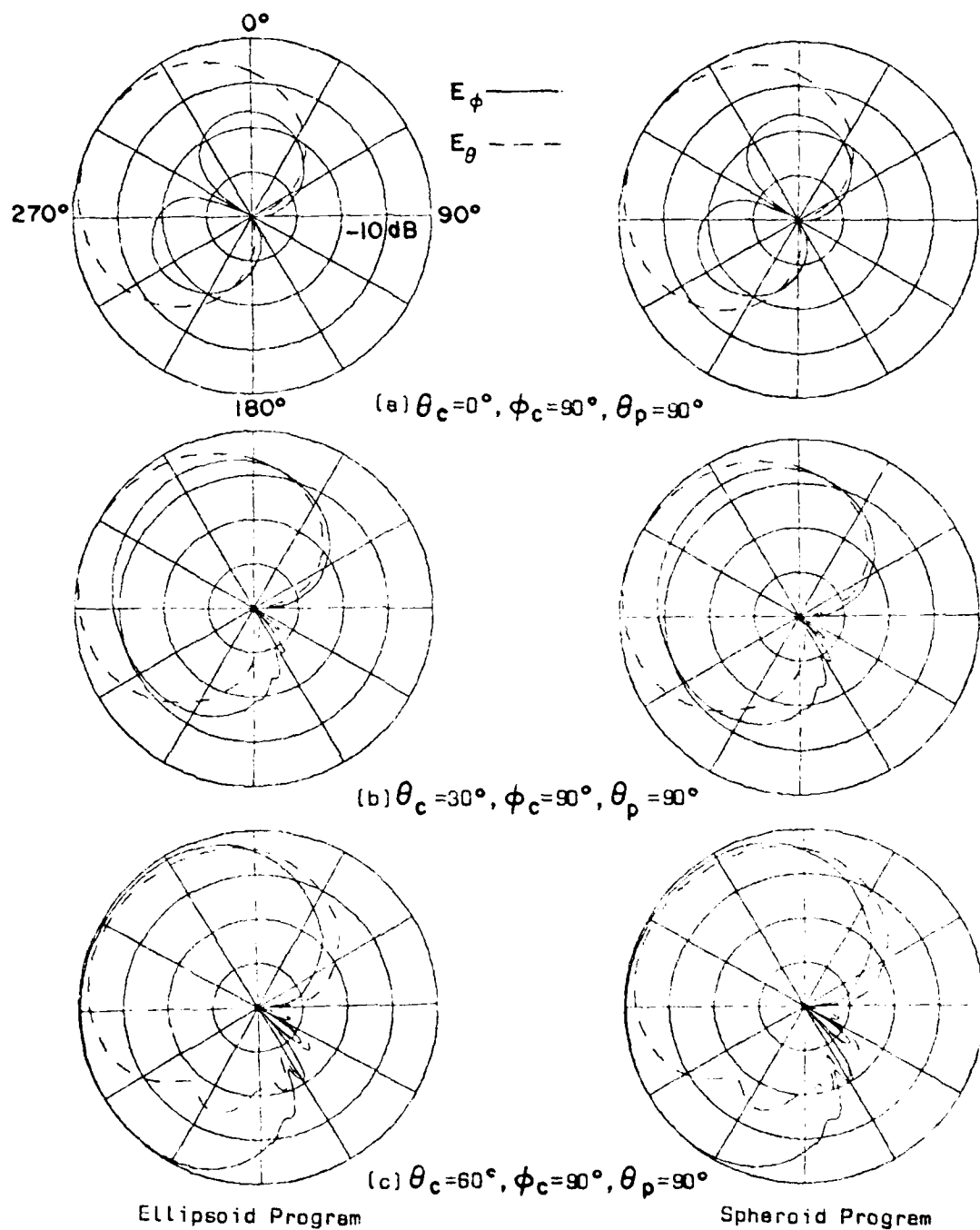
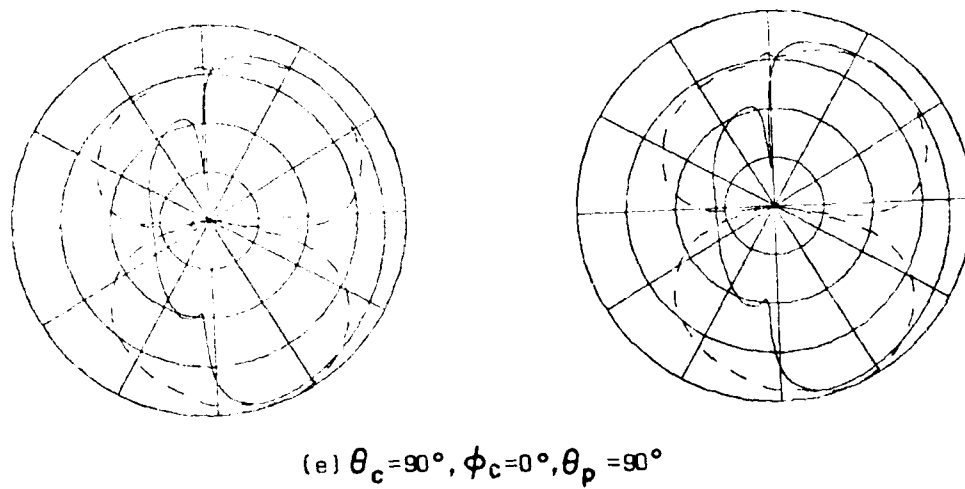
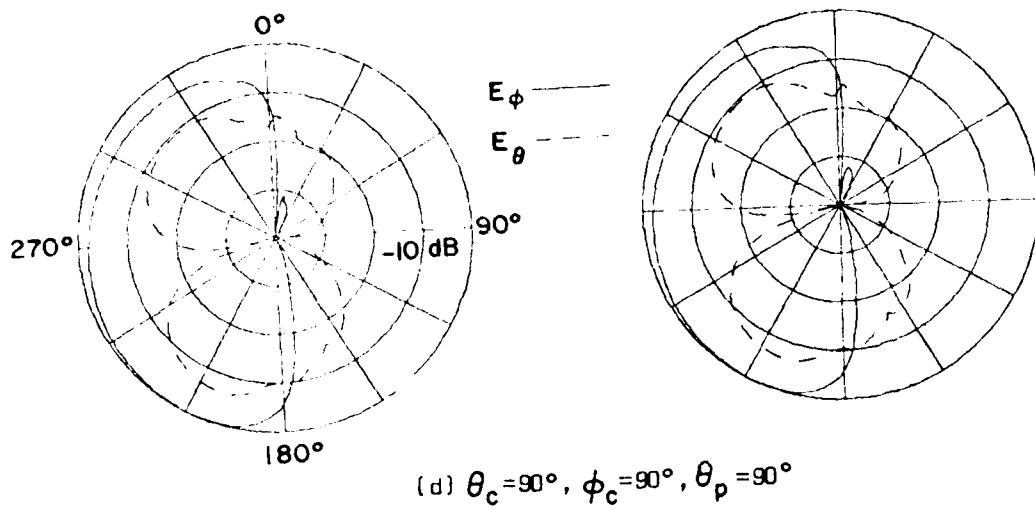


Figure 19. Comparison of radiation patterns for a circumferential slot mounted at  $\phi_s = 30^\circ, \theta_s = 30^\circ$  on a  $2\lambda \times 10\lambda$  spheroid.





Ellipsoid Program

Spheroid Program

Figure 19. (continued)

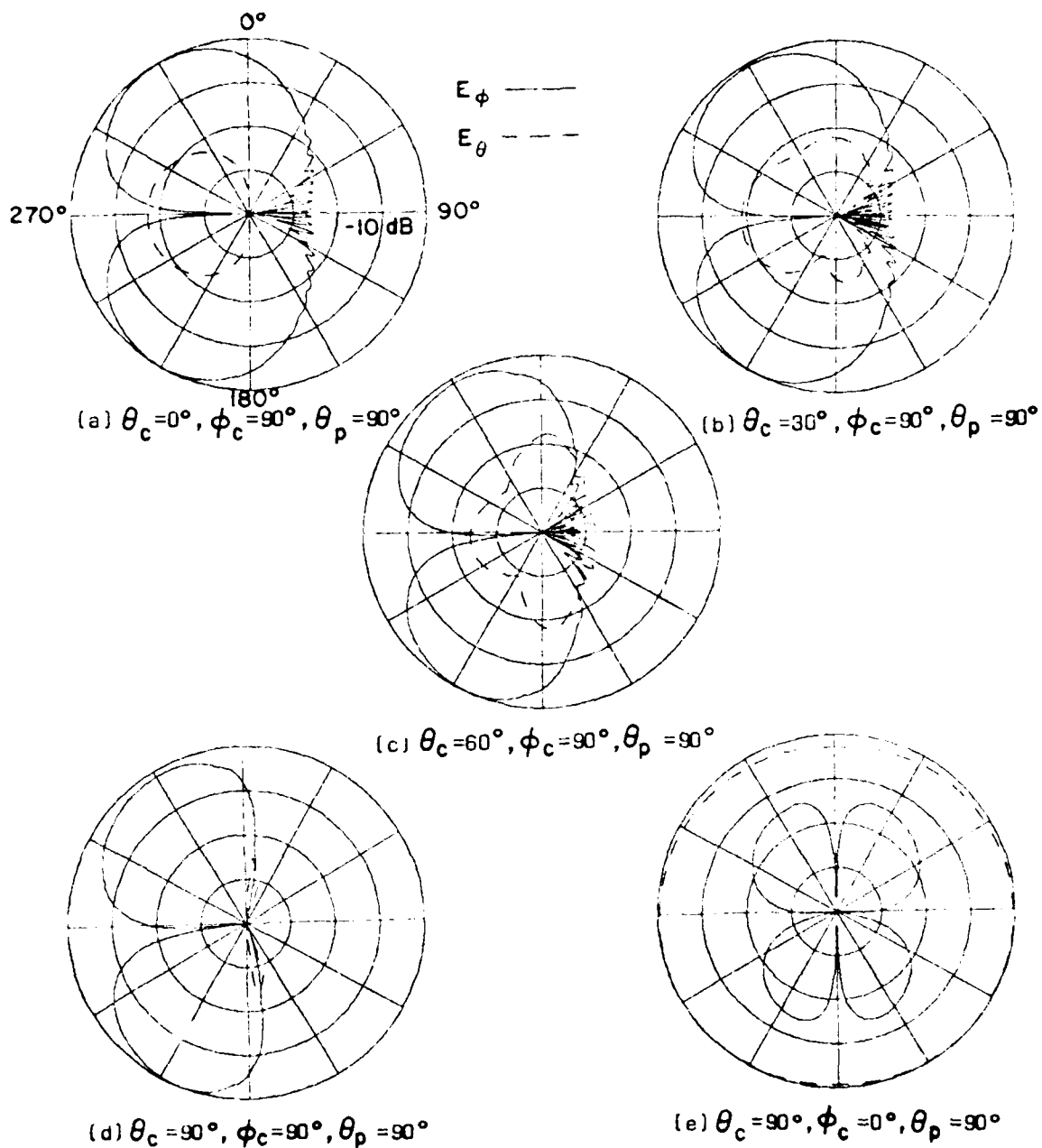


Figure 20. Radiation patterns for  $R_t = 15\lambda$  for a short monopole mounted at  $\phi_s = 0^\circ$ ,  $\theta_s = 60^\circ$  on a  $2\lambda \times 4\lambda \times 10\lambda$  ellipsoid.

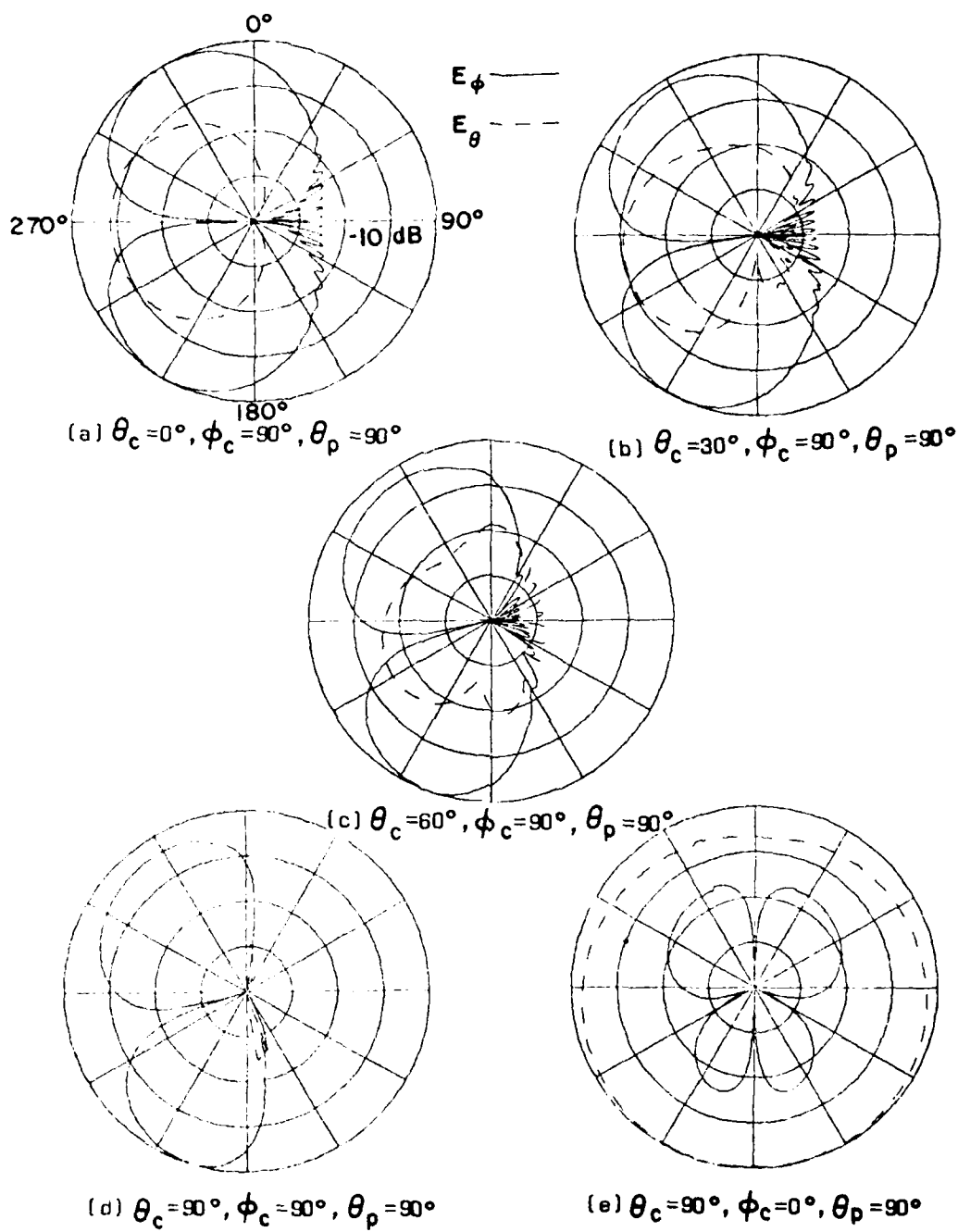


Figure 21. Radiation patterns for a short monopole mounted at  $\phi_s = 0^\circ, \theta_s = 30^\circ$  on a  $2\lambda \times 4\lambda \times 10\lambda$  ellipsoid.

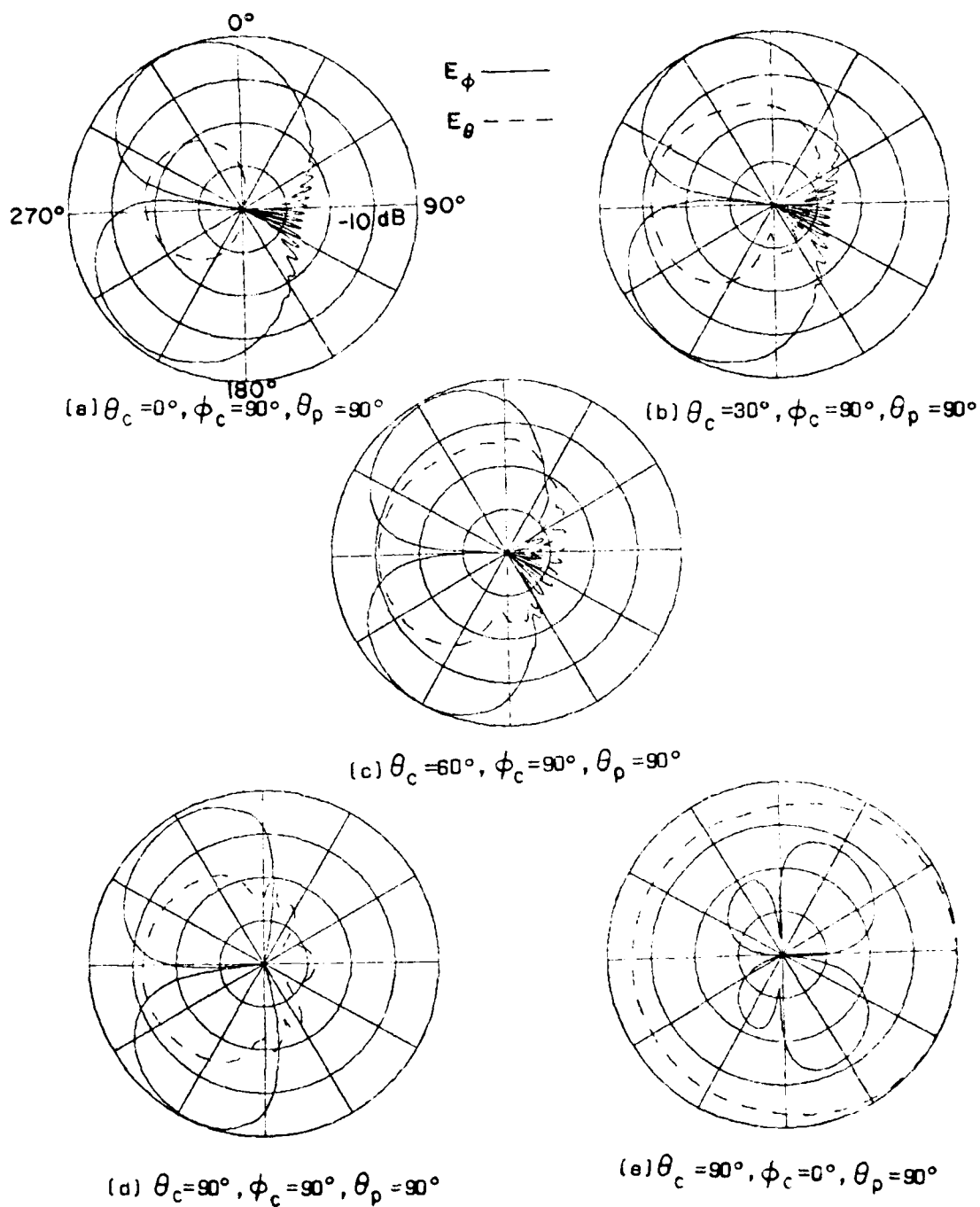


Figure 22. Radiation patterns for a short monopole mounted at  $\phi_s = 30^\circ, \theta_s = 60^\circ$  on a  $2\lambda \times 4\lambda \times 10\lambda$  ellipsoid.

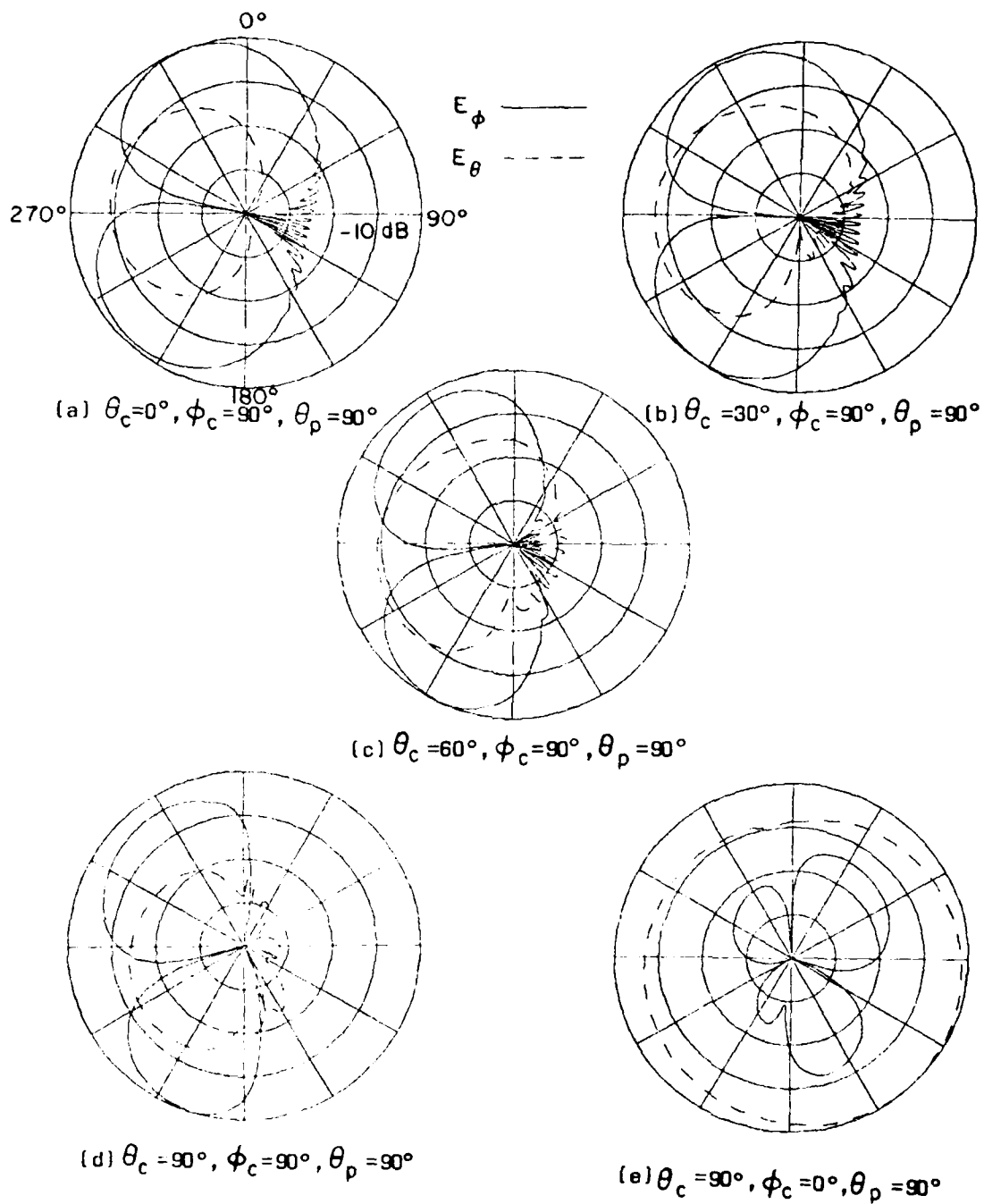


Figure 23. Radiation patterns for a short monopole mounted at  $\phi_s = 30^\circ, \theta_s = 30^\circ$  on a  $2\lambda \times 4\lambda \times 10\lambda$  ellipsoid.

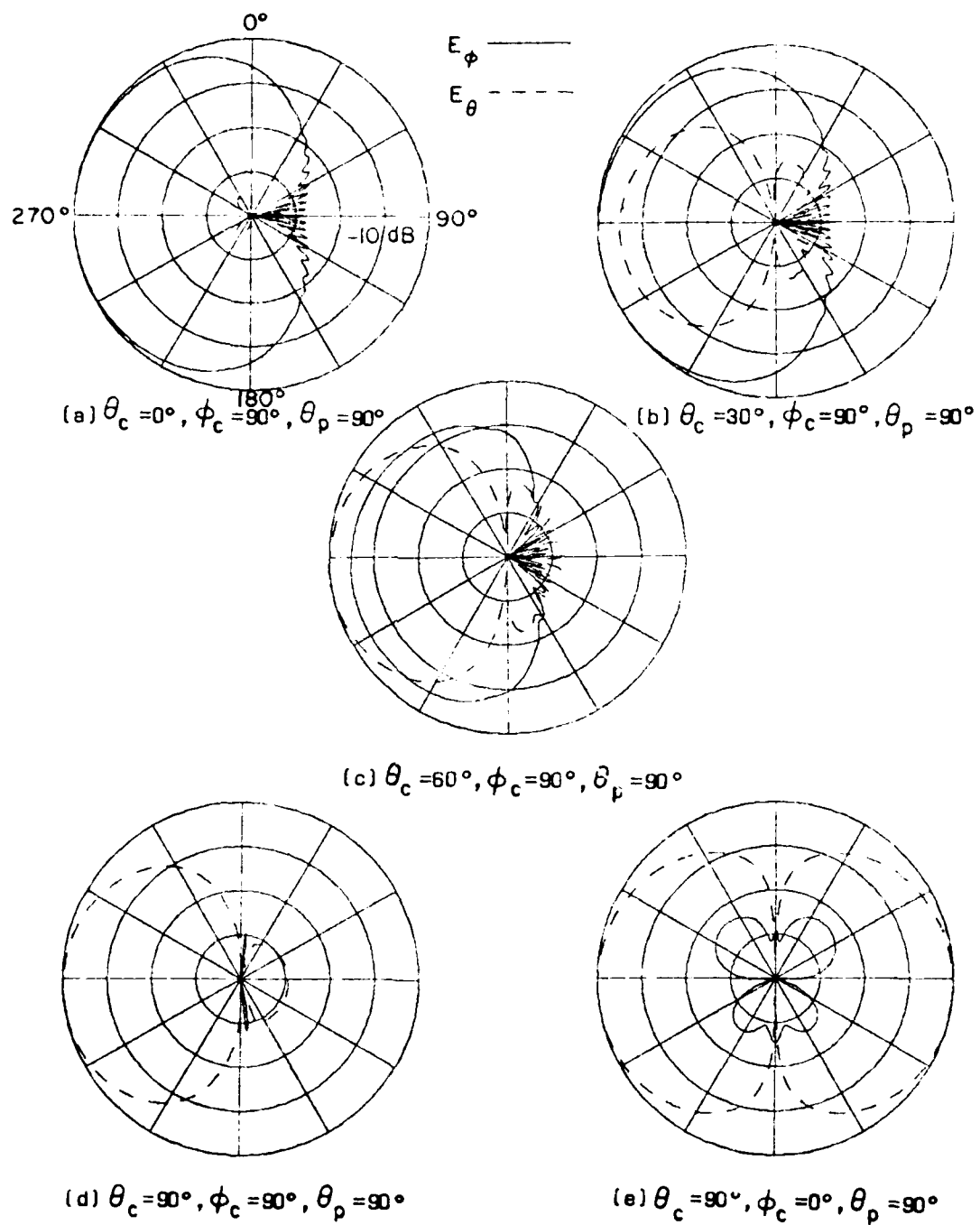


Figure 24. Radiation patterns for an axial slot mounted at  $\phi_s = 0^\circ$ ,  $\theta_s = 60^\circ$  on a  $2\lambda \times 4\lambda \times 10\lambda$  ellipsoid.

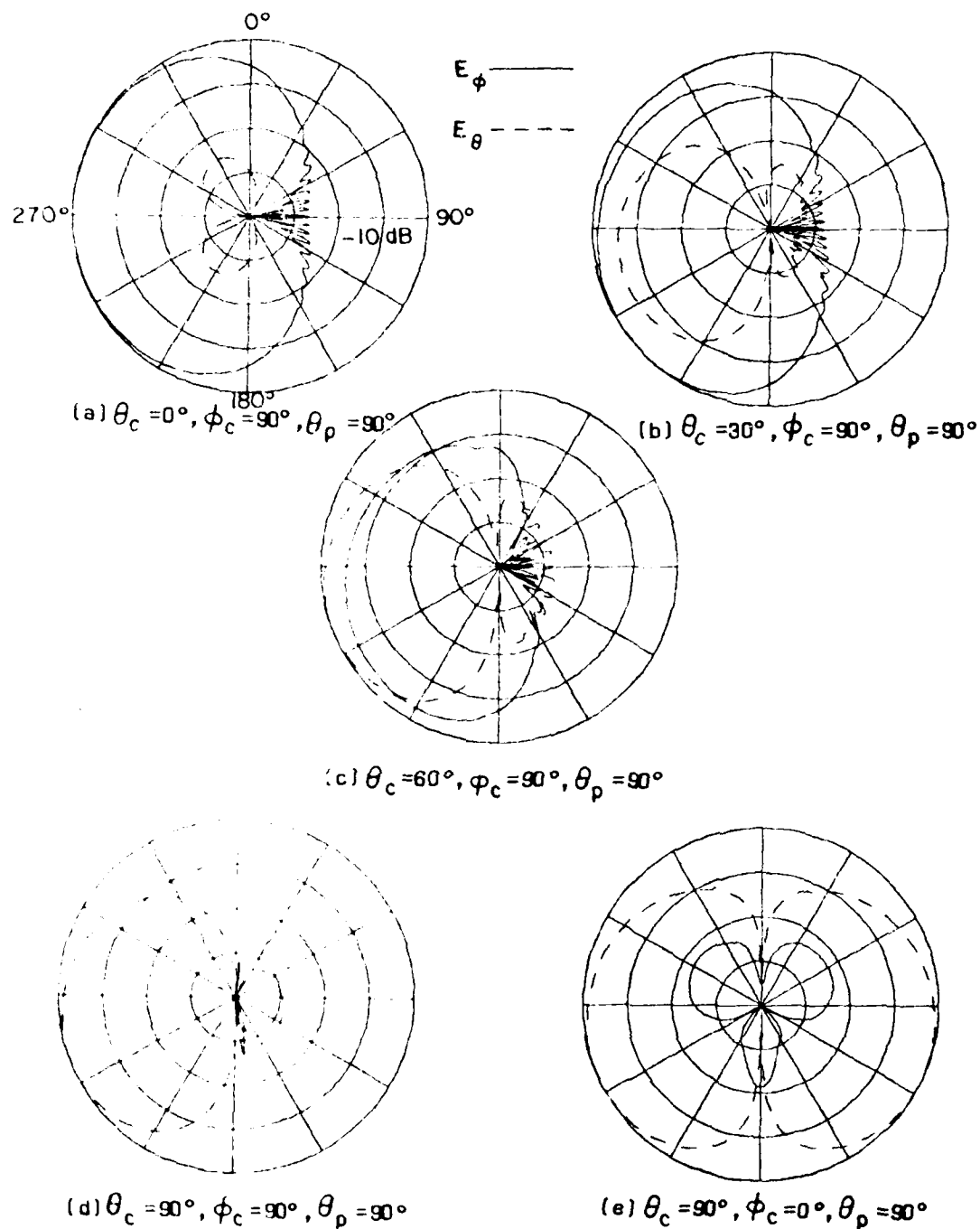


Figure 25. Radiation patterns for an axial slot mounted at  $\theta_s = 0^\circ, \phi_s = 30^\circ$  on a  $2\lambda \times 4\lambda \times 10\lambda$  ellipsoid.





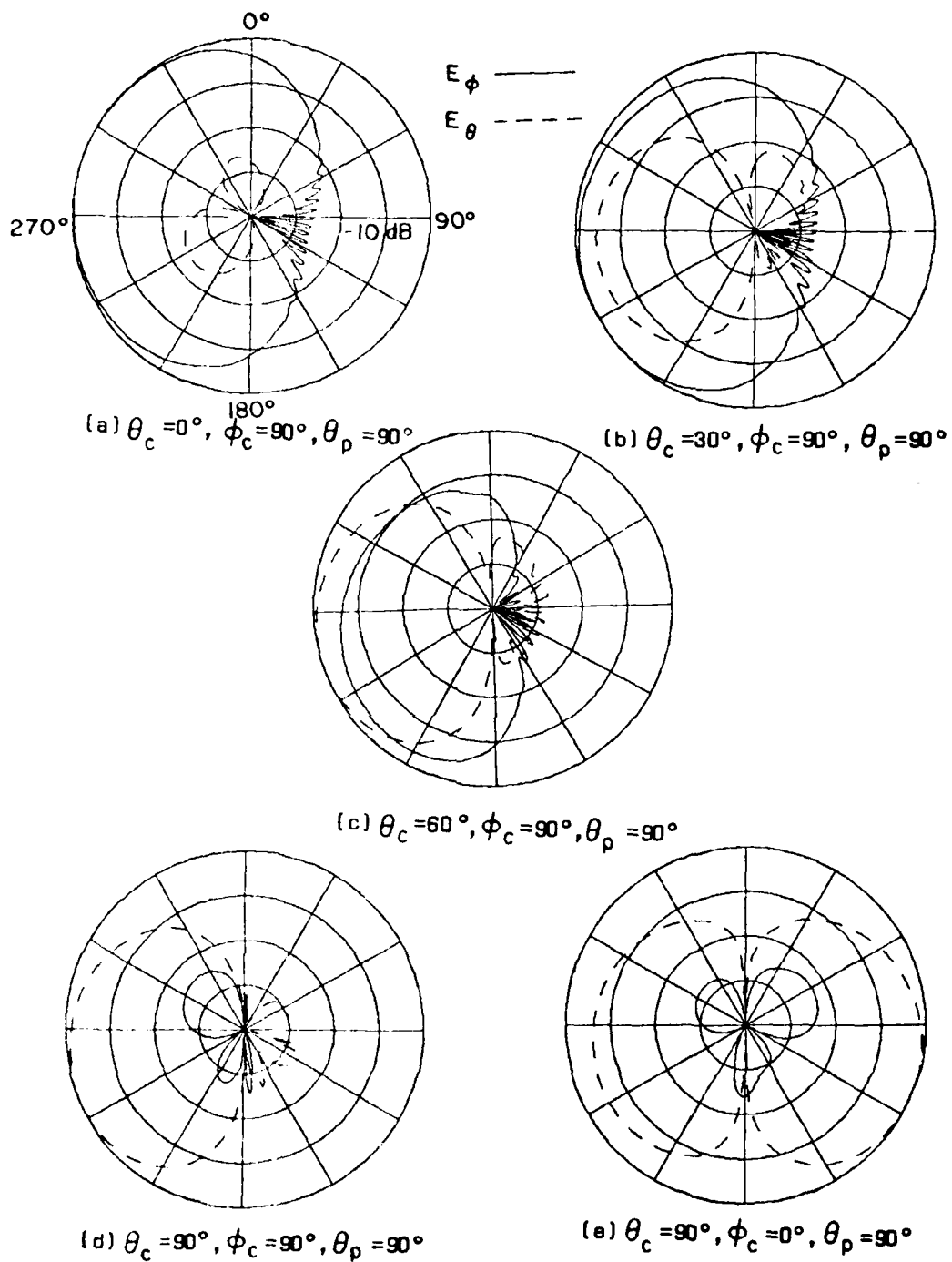


Figure 27. Radiation patterns for an axial slot mounted at  $\phi_s = 30^\circ, \theta_s = 30^\circ$  on a  $2\lambda \times 4\lambda \times 10\lambda$  ellipsoid.

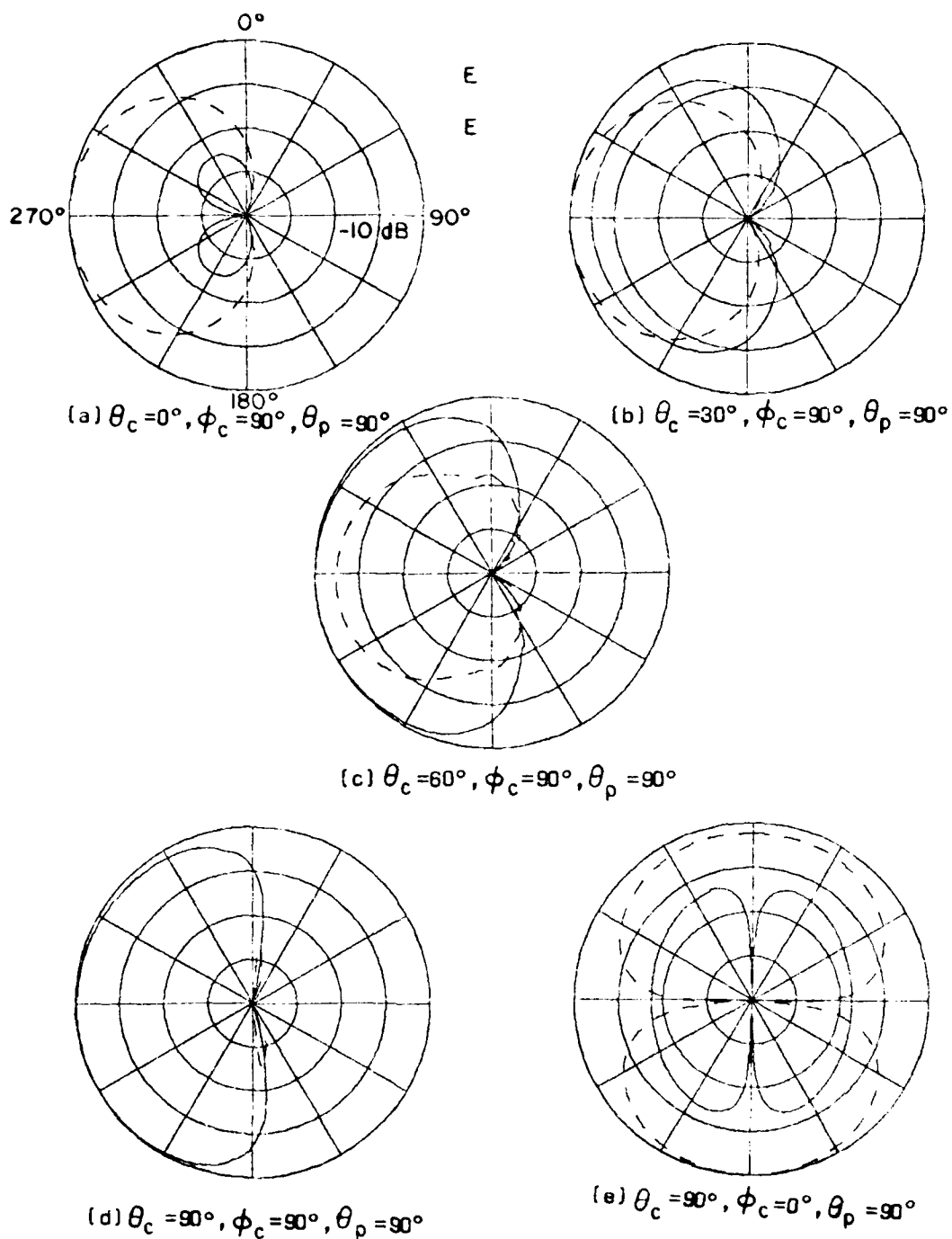


Figure 28. Radiation patterns for a circumferential slot mounted at  $\phi_s = 0^\circ$ ,  $\theta_s = 60^\circ$  on a  $2\lambda \times 4\lambda \times 10\lambda$  ellipsoid.

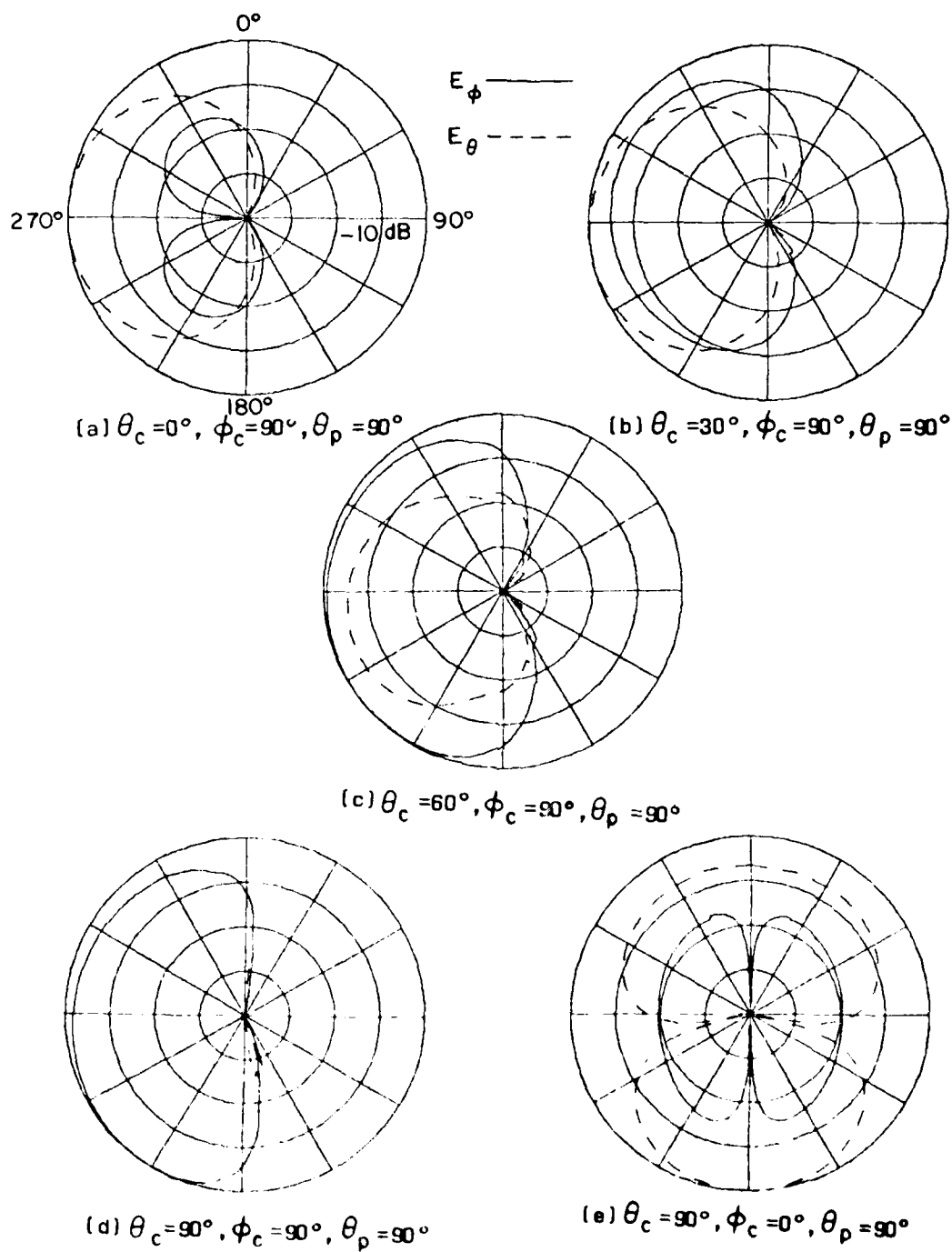


Figure 29. Radiation patterns for a circumferential slot mounted at  $\theta_s = 0^\circ, \phi_s = 30^\circ$  on a  $2\lambda \times 4\lambda \times 10\lambda$  ellipsoid.

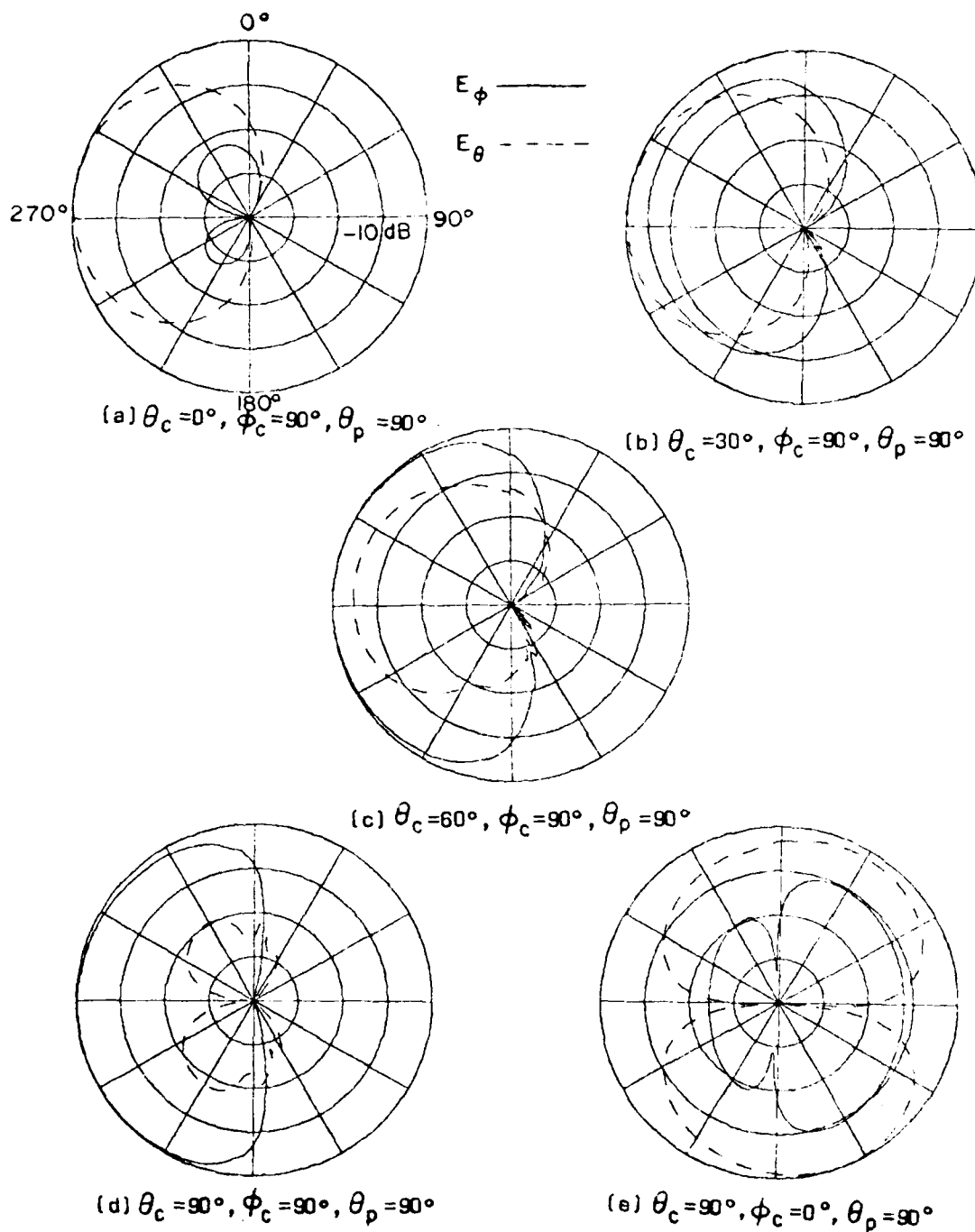


Figure 30. Radiation patterns for a circumferential slot mounted at  $\phi_s = 30^\circ, \theta_s = 60^\circ$  on a  $2\lambda \times 4\lambda \times 10\lambda$  ellipsoid.

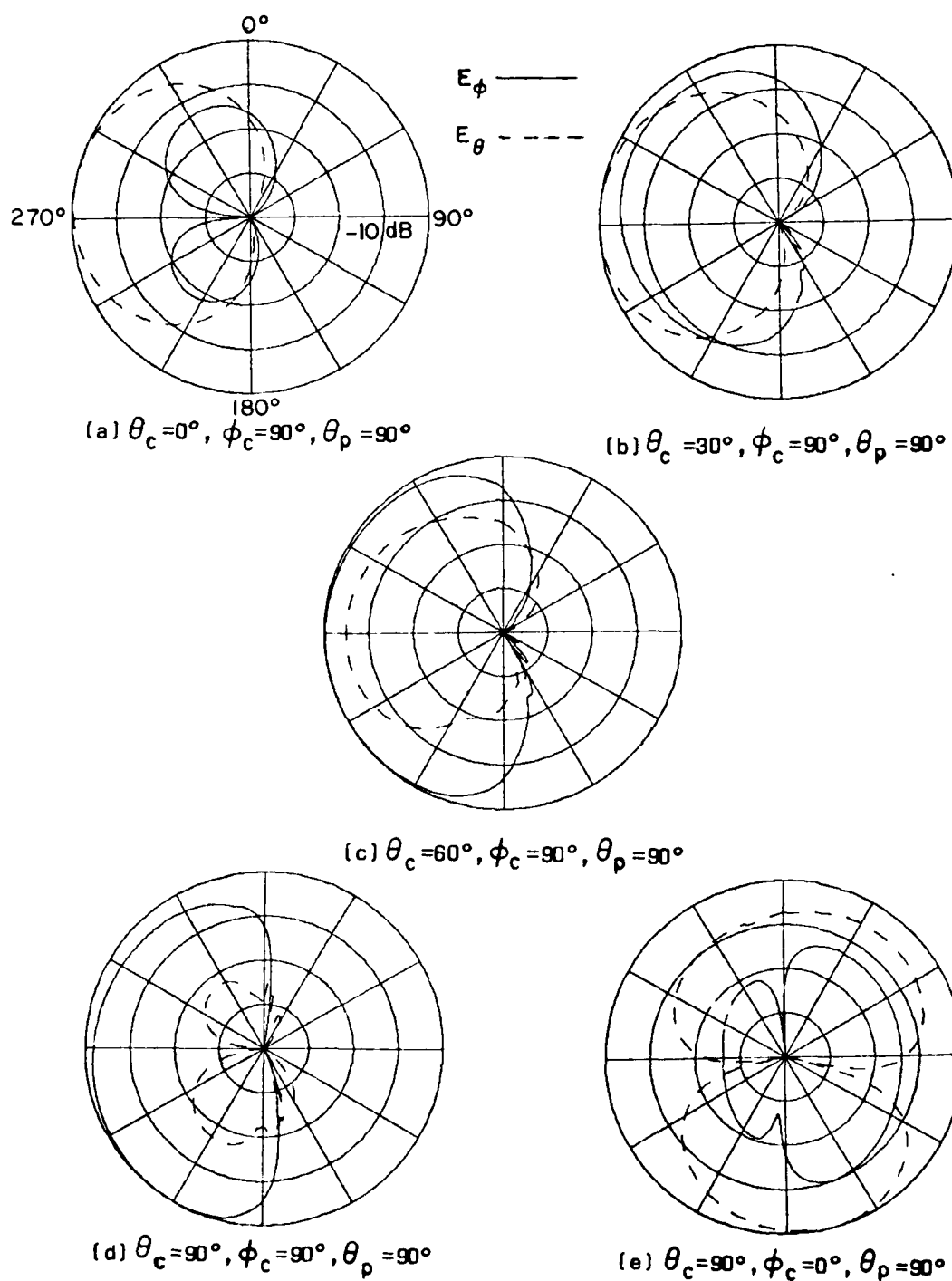


Figure 31. Radiation patterns for a circumferential slot mounted at  $\phi_s = 30^\circ, \theta_s = 30^\circ$  on a  $2\lambda \times 4\lambda \times 10\lambda$  ellipsoid.

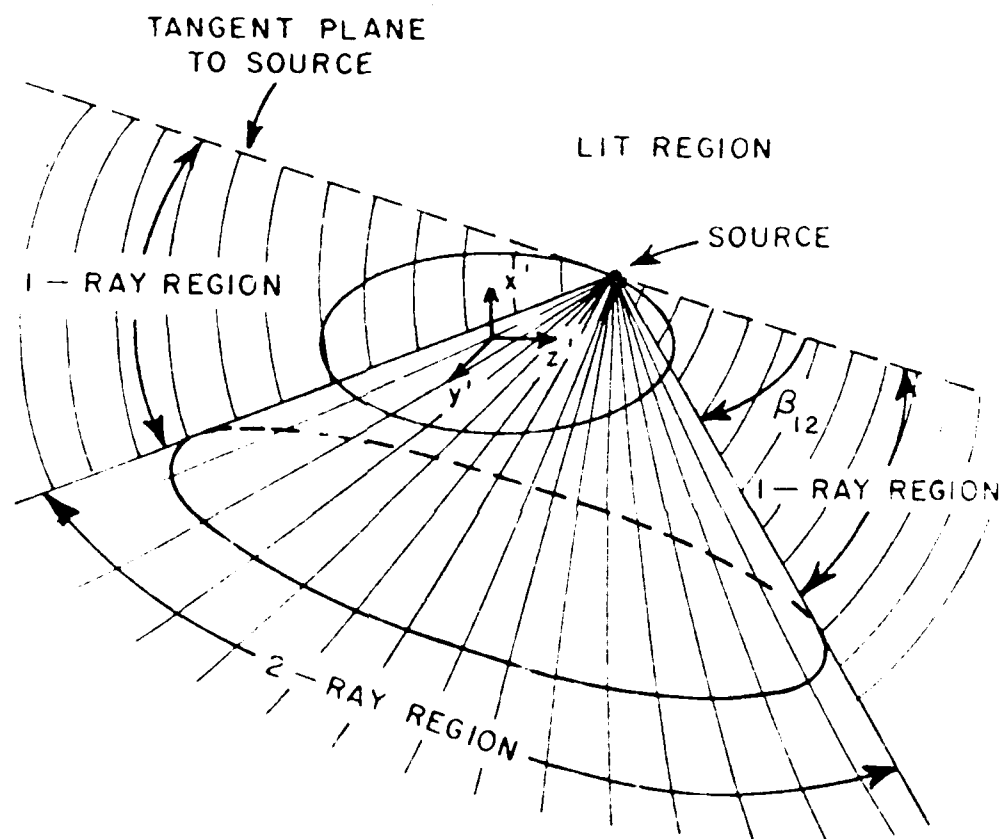


Figure 32. Cone boundary used to define terms to be included in the shadow region.

#### REFERENCES

- [1] P.H. Pathak, N. Wang, W.D. Burnside, and R.G. Kouyoumjian, "A Uniform GTD Solution for the Radiation from Sources on a Convex Surface", IEEE Trans. and Prop., Vol. AP-29, No. 4, July 1981.
- [2] J.G. Kim, W.D. Burnside and N. Wang, "Geodesic Solution for an Antenna Mounted on an Ellipsoid", Report 713321-3, The Ohio State University ElectroScience Laboratory, Department of Electrical Engineering; prepared under Contract No. N00019-80-PR-RJ015 for Naval Air Systems Command, March 1982.
- [3] J.G. Kim and W.D. Burnside, "Geodesic Paths for Side-Mounted Antenna on an Ellipsoid Model", Report 714215-1, The Ohio State University ElectroScience Laboratory, Department of Electrical Engineering; prepared under Contract No. N00019-81-C-0424 for Naval Air Systems Command, October 1982.
- [4] J.G. Kim and W.D. Burnside, "Radiation Patterns of an Antenna Mounted on the Mid-Section of an Ellipsoid", Report 714215-2, The Ohio State University ElectroScience Laboratory, Department of Electrical Engineering; prepared under Contract No. N00019-81-C-0424 for Naval Air Systems Command, July 1983.
- [5] H. Chung, W.D. Burnside, and N. Wang, "The Near Field Radiation Patterns of a Spheroid-mounted Antenna", Report 712527-2, The Ohio State University ElectroScience Laboratory, Department of Electrical Engineering; prepared under Contract No. N00019-81-C-0050 for Naval Air Systems Command, January 1980.

END

DATE  
FILMED

8 - 83

DTIC